EUROPEAN ORGANIZATION FOR NUCLEAR RESEARCH


# ERRATUM

## INELASTIC INTERMEDIATE STATES IN PROTON-DEUTERON AND DEUTERON-DEUTERON ELASTIC COLLISIONS AT THE ISR

G. Goggi et al.

(To be published in Nuclear Phys. B)

*On p. 9, Eq. (4.2) should read*

$$\langle\psi_1\psi_2|\hat{F}_{dd}|\psi_1\psi_2\rangle = \hat{F}_{Glauber} + \frac{8i}{\pi p_\ell} S_0(q/2) \int d^2q_{1T}\, dM^2\, \Delta F_6^{tot}(s+i\varepsilon,\, s+i\varepsilon;\, M^2) S_0(\vec{q}_{1T}, q_{1L}) -$$

$$- \frac{16}{\pi^2 p_\ell^2} \int d^2q_{1T}\, f\left(-\vec{q}_{1T} + \frac{\vec{q}}{2}\right) S_0(q_{1T}) \int d^2q_{2T}\, dM^2\, \Delta F_6^{tot}(s+i\varepsilon,\, s+i\varepsilon;\, M^2) S_0(\vec{q}_{2T}, q_{2L}) \,.$$

*and Eq. (4.3) should read*

$$\Delta F_6^{tot}(s+i\varepsilon,\, s+i\varepsilon;\, M^2) = -e^{-(b_0/2)(q^2/4)} \frac{d\sigma}{dt dM^2} \frac{p_\ell^2}{\pi}$$

*On p. 20, the footnote to Table 4 should be deleted and the caption should read*

> Parameters of the triple-Regge expansion of Field and Fox [32]. The notation is the same as in eqs. (3.3) and (3.4). The first four parameters give the behaviour of the vertex function $V_{iim}V^2_{NNi} = (V_1\, e^{\beta_1 t} + V_2\, e^{\beta_2 t})(-t)$.

*On p. 21, the caption to Table 5 should read*

> Parameters of the triple-Regge expansion of Roy and Roberts [33]. In this case $V_{iim}V^2_{NNi} = V_1\, e^{\beta_1 t} + V_2\, e^{\beta_2 t}$

*In the first column of this table, $V_1$ and $V_2$ should be in units of $[mb/(GeV)^2]$.*

*On p. 22, the caption to Table 6 should read*

> Parameters of the triple-Regge expansion of Dakhno [34]. In this case the vertex function is the same as in Table 4.

Geneva - 8 November 1978

EUROPEAN ORGANIZATION FOR NUCLEAR RESEARCH

# INELASTIC INTERMEDIATE STATES IN PROTON-DEUTERON AND DEUTERON-DEUTERON ELASTIC COLLISIONS AT THE ISR

G. Goggi*)
CERN, Geneva, Switzerland

M. Cavalli-Sforza**), C. Conta, M. Fraternali, G.C. Mantovani and F. Pastore
Istituto di Fisica Nucleare, Università di Pavia
and Istituto Nazionale di Fisica Nucleare, Sezione di Pavia, Italy

G. Alberi
Istituto di Fisica Teorica, Università di Trieste
and Istituto Nationale di Fisica Nucleare, Sezione di Trieste, Italy

## ABSTRACT

We present experimental results on proton-deuteron and deuteron-deuteron elastic scattering measured at the two highest ISR energies, $\sqrt{s}$ = 53 GeV and $\sqrt{s}$ = 63 GeV. The data cover the single and multiple scattering regions over a wide interval of four-momentum transfer t. In both reactions we find clear evidence for a substantial t-dependent contribution of inelastic intermediate states in the multiple scattering region, as well as in single scattering. In the analysis we use the Glauber multiple-scattering theory extended to include inelastic shadow effects. This extension of the basic theory contains as input a triple Regge parametrization describing the high-mass inclusive spectrum. The analysis of inelastic corrections to multiple scattering on deuterons at high energies is shown to provide a sensitive test of different parametrizations of inclusive production in proton-proton collisions.

Geneva - 16 October 1978

(Submitted to Nuclear Phys. B)

---

*) On leave from the Istituto di Fisica Nucleare, Università di Pavia and INFN, Sezione di Pavia, Italy.

**) Present address: Princeton University, Princeton, NJ, USA.

## 1. INTRODUCTION

Several experiments were performed in the late sixties to measure the differential cross-section for $\pi$d [1] and pd [2] elastic scattering in the 1-10 GeV region, the main idea being to test in a simple case the Glauber [3] eikonal approach to hadron-nucleus scattering and to extract information on the real part of the hadron-nucleon amplitude.

For a two-nucleon system like the deuteron, Glauber theory describes [4] elastic scattering with just two terms: single scattering, where one nucleon interacts and the other is a spectator, and double scattering, where both nucleons take part in the process. These two terms have different signs and interfere destructively. Since the first term is proportional to the hadron-nucleon amplitude and the second to its square, the hadron-deuteron amplitude is sensitive to the real part in the region of the interference minimum [5]. However, as well known [6], one gets the differential cross-section by adding incoherently to the amplitude squared another term associated with the D-component of the deuteron wave function. As a consequence, the sensitivity to the real part is reduced to impractical levels, at least for unpolarized deuterons.

Glauber theory was able to explain the gross features of the experimental hadron-deuteron angular distribution, identifying the low-t and high-t regions as single and double scattering, respectively. There is, however, at least one case [7] which shows a systematic discrepancy between theory and experiment at high momentum transfer. Many theoretical papers [8] indicated the deuteron recoil corrections as a possible explanation for this discrepancy and a recent paper [9] also gave the right order of magnitude by simply including in the theory the proper calculation of the Jacobian $d\Omega_{lab}/dt$. Other explanations are available [10], but this discrepancy should be a transient phenomenon, vanishing with increasing energy; a pd experiment at 24 GeV/c [11] seems to confirm this expectation.

Two other experiments were recently performed at Fermilab [12] and at the CERN Intersecting Storage Rings (ISR) [13], measuring the pd elastic cross-section

between 50 and 400 GeV/c and at $\sqrt{s}$ = 53 GeV, respectively. However, the t-range explored by these experiments does not sufficiently extend in the interference and double scattering regions to allow for a detailed test of the theory.

Even if dd elastic scattering is the second in simplicity, and therefore suitable for testing Glauber theory, not much effort was spent to explore it experimentally. A first experiment [14] investigated the energy region from 680 to 2120 MeV/c of incident deuteron momentum, and a second one [15] was performed at 7.9 GeV/c. Both experiments, however, have not enough statistics at large momentum transfer for performing any significant test.

This was very unfortunate, because in dd scattering, contrary to the pd case, the dip [16,17] caused by the interference between single and double scattering is not completely filled by the D-wave contribution, since it occurs at a lower value of $|t|$. In addition, for $-t > 0.3$ GeV$^2$ there is still interference between double and triple scattering, which also is sensitive to the real part.

The injection and acceleration of deuterons in the ISR made it possible to investigate pd and dd elastic scatterings at the highest available energies and to perform a more refined experiment on dd elastic scattering.

The relatively high luminosities achieved and the background-free running conditions allowed the measurement with good statistical accuracy of elastic differential cross-sections in the t-range from about 0.07 GeV$^2$, a practical lower limit imposed by vacuum chamber geometry, up to about 2 GeV$^2$. These measurements, covering extensively the single and multiple scattering regions, were performed at the two highest ISR energies, at which deuteron beams could be easily stored and accelerated.

Both for the pd and the dd case, the theoretical analysis of the data required the introduction of inelastic intermediate states (IIS) [18] in the Glauber formulae. We also found that the results are sensitive to the type of the Regge parametrization for the $(d\sigma/dtdM^2)(pp \to pX)$ one uses as input for the calculation of the inelastic shadow effect. In particular, for the dd case we found that there is a substantial cancellation between the IIS corrections in the double and the triple

scattering terms, which makes the dd elastic cross-section an even more sensitive test of the Regge parametrization. Preliminary results on these subjects have already been published [19].

The organization of this paper is as follows. In section 2 we discuss the details of the experimental analysis of dd and pd elastic scattering. In sections 3 and 4 we recall the basic Glauber formulae for pd and dd collisions, respectively, with the inclusion of IIS. In section 5 we present our experimental results, comparing them with lower energy data and with the theoretical curves, and discuss the sensitivity to the Regge parametrization. Our conclusions are given in section 6.

## 2. EXPERIMENTAL TECHNIQUE

In this section we describe the features of the experimental apparatus used to detect elastic scattering events and the specific trigger conditions defining the selection criteria. We then discuss the properties of the off-line event reconstruction and the characteristics of the final event sample. Details concerning aspects of the experimental technique have also been described in recent publications [19].

### 2.1 Apparatus and trigger

The data on pd and dd elastic scattering at the two c.m. energies of 53 GeV and 61 GeV were collected in four runs during which deuterons were accumulated in one or both ISR rings at $p_{beam}$ = 26.6 and 31.45 GeV/c, respectively. Deuteron currents up to 8 A were stored with peak luminosities of $10^{30}$ $cm^{-2}$ $s^{-1}$; the ISR performance during the deuteron runs achieved a beam lifetime consistent with the interaction rate at the eight crossing regions around the ring.

Elastic scattering events were detected in two narrow angular regions in the forward telescopes of the Split Field Magnet (SFM) detector.

The SFM has been described in detail elsewhere [20]; a plan view of the detector is shown in fig. 1. It consists of a set of multiwire proportional chambers (about 70 000 wires) surrounding the interaction region and covering almost a $4\pi$ solid angle. A first set of chambers covers the central region at large angles;

a second set covers smaller angles in the two symmetric forward telescopes. Additional chambers in the compensator magnets allow detection of particles down to about 8 mrad to the beams with a momentum resolution $\Delta p/p$ of about $\pm 0.07$ for elastic scattering at $p_{beam} = 26.6$ GeV/c. The steepness of the deuteron form factor confines the region of interest for elastic scattering at very small values of t. In fact it is around $-t = 0.3$ GeV$^2$ for pd and $-t = 0.2$ GeV$^2$ for dd scattering that the interference between single and multiple scattering is maximal. As a consequence, our elastic trigger was confined to the small angular regions subtended by the compensator telescopes. Events were required to have one charged track in each telescope with at least three space-points measured and having projections collinear within 8 mrad in the non-bending plane. Different scaling factors could be applied to different t-intervals to enrich our high-t sample of events. These triggers were recorded for off-line reconstruction and analysis together with monitor counts from a downstream scintillation hodoscope and other detector information.

The off-line reconstruction chain consisted of three standard programs performing pattern recognition, track fitting in the magnetic field to a common vertex, and a kinematical fit. The chain was preceded by a filter which selected events according to the same criteria as for the trigger but with improved spatial resolution. After the four-constraint kinematical fit, events corresponding to a confidence level greater than 0.01 were retained in the final sample.

## 2.2 Characteristics of the event sample

At a topological level the main background to the elastic events of interest is given by the deuteron break-up reaction. Given the large deuteron momentum in the laboratory, the momentum measurement on the final state particles separates easily the break-up products, which peak at half the beam momentum, from genuine elastic events. This is clearly seen in fig. 2, where the correlation between the two measured final state momenta is shown for pd and dd scattering at $\sqrt{s} = 53$ GeV. The regions of single and double break-up appear completely separated from the elastic scattering region. The other main sources of background are $\pi^0$ production and beam scattering on the residual gas. Concerning the former, it has to be

noted that mainly multipion coherent production may contribute to the background and this mechanism is kinematically suppressed to a large extent by the deuteron form factor and by the collinearity constraint in the event reconstruction. Single coherent $\pi^0$ production is in fact inhibited by isospin invariance at the deuteron vertices. Beam-gas contamination was below the 1% level in all runs, consistent with no effect associated with the beam lifetime. No background subtraction was performed; the main characteristics of the data sample are given in table 1.

The acceptance of the detector and of the off-line reconstruction chain was studied with Monte Carlo methods. This simulation took into account the beam parameters, the detailed detector geometry, and absorption and scattering in the ISR vacuum chamber and in the detector material. Trigger conditions, proportional chamber inefficiencies, and losses in the reconstruction chain were also taken into account.

The acceptance was found to be an essentially constant function of t from $-t = 0.05$ GeV$^2$ to values in excess of 2 GeV$^2$. It has been separately calculated at the two ISR energies and the results were found to scale in $t/p^2$ as expected from pure geometrical arguments.

The reliability of the simulation has been extensively checked by comparing $\chi^2$ and collinearity distributions of real and Monte Carlo events in different intervals of t with excellent agreement in all cases [19]. The same set of simulated events was used to investigate the experimental t-resolution

$$(dt)^2 = 2t \left[ t\left(\frac{dp}{p}\right)^2 + p^2 \, (d\theta)^2 \right] , \qquad (2.1)$$

where the errors on angles and momenta are in turn smooth functions of t due to the effect of multiple scattering in the vacuum chamber walls. It was found that $\Delta t/t = 7\%$ at the position of the interference minimum in dd scattering with a slow t-dependence as approximately $1/\sqrt{t}$.

After applying acceptance corrections and a normalization factor to get absolute differential cross-sections, a t-dependent systematic uncertainty was combined with the statistical errors of the data. This uncertainty is essentially

contributed by the absorption in the ISR corrugated vacuum chamber walls, on the average $4 \times 10^{-3}$ absorption lengths thick for normal traversal. We have determined the absorption uncertainty from an estimated 15% uncertainty in the path length of the particles traversing the vacuum chamber. The over-all systematic uncertainty on the data is reported in table 1.

## 3. THEORY FOR PROTON-DEUTERON SCATTERING AT VERY HIGH ENERGIES

The well-known Glauber [3] formula for hadron-deuteron scattering is obtained assuming the nucleons of the deuteron as fixed scattering centres, their spatial distribution being described by the deuteron wave function. Clearly this is true in very good approximation in the deuteron rest system at small momentum transfers. The scattering amplitude [4], neglecting the difference between neutron and proton, is given by

$$\langle\psi|F_{pd}|\psi\rangle = 2f(q)\langle\psi|\ e^{i\vec{q}\cdot\vec{s}/2}\ |\psi\rangle + \\ + \frac{i}{2\pi p_\ell}\int d^2q'_T\langle\psi|\ e^{i\vec{q}'_T\cdot\vec{s}}\ |\psi\rangle\ f\left(-\vec{q}'_T + \frac{\vec{q}}{2}\right)f\left(\vec{q}'_T + \frac{\vec{q}}{2}\right), \qquad (3.1)$$

where $p_\ell$ is the incident proton momentum in the deuteron rest frame, q the transferred momentum, s the transverse part of the internal deuteron coordinate, and $q'_T$ the transverse component of the internal momentum transfer to the deuteron. We define

$$\langle\psi|\ e^{i\vec{q}\cdot\vec{r}}\ |\psi\rangle = \hat{S}(q) = S_0(q) - \left[3(\vec{J}\cdot\hat{q})^2 - 2\right]S_2(q)$$

$$S_0(q) = \int_0^\infty j_0(qr)\left[u^2(r) + w^2(r)\right]dr$$

$$S_2(q) = \sqrt{2}\int_0^\infty j_2(qr)\left[u(r)w(r) - \frac{w^2(r)}{\sqrt{8}}\right]dr\ ,$$

u and w being the S and D radial wave functions of the deuteron and J its angular momentum. The first term in eq. (3.1), corresponding to single scattering, can be derived [21] from the Feynman graph of fig. 3a; the second represents double scattering and is related to the diagram of fig. 3b.

As originally suggested by Abers et al. [22], the diagram of fig. 3b can be complicated by the internal production of one or several pions (fig. 4a): although this production is suppressed by the longitudinal momentum transfer $q_L = (M^2 - m^2)/2p_\ell$ at intermediate energies, it is certainly present at extremely high energies.

Gribov [23] calculated this effect assuming Pomeron exchange as the dominant production mechanism (fig. 4b) by relating the product of the multipion amplitudes to the inclusive cross-section. Similarly, using unitarity for the Reggeon-hadron amplitude, one can calculate [24] the effect including also other Reggeized exchanges, and using the triple Regge coupling determined by the analysis of the inclusive cross-section (fig. 4c). However, fig. 4c is a Feynman diagram, whereas the Müller diagram is a unitarity diagram: this gives a difference in phase, namely a minus sign for the Pomeron at $q = 0$, which modifies substantially the relative contribution of the various terms [25].

If the produced mass is small, one can approximate the intermediate inelastic amplitudes in terms of resonance production by simply replacing in the second term of formula (3.1) the scattering amplitudes by the production amplitudes. The modified scattering amplitude becomes [18]

$$\langle\psi|F_{pd}|\psi\rangle = F_{Glauber} +$$

$$+ \frac{i}{2\pi p_\ell} \sum_m \int d^2q'_T \langle\psi| \, e^{i\vec{q}'_T\cdot\vec{s}+iq_Lz} \, |\psi\rangle f_n\left(-\vec{q}'_T + \frac{\vec{q}}{2}\right) f_n\left(\vec{q}'_T + \frac{\vec{q}}{2}\right) +$$

$$+ \frac{i}{2\pi p_\ell} \sum_{ijm} \eta_j \, e^{-i\pi\beta_j(q^2/4)} \int d^2q'_T \, dM^2 \, \langle\psi| \, e^{i\vec{q}'_T\cdot\vec{s}+iq_Lz} \, |\psi\rangle \, \Delta F_6^{ijm}(s+i\varepsilon, s-i\varepsilon; M^2) \, , \tag{3.2}$$

where $\vec{q}'_T$ and $q_L$ are the transverse and longitudinal components of the internal momentum transfer, i, j, m are the Regge pole indices (see fig. 4c), and $\Delta F_6$ is the discontinuity of the corresponding six-point amplitude; this is related to the contribution to the inclusive cross-section for $pp \to pX$

$$\Delta F_6^{ijm}(s + i\varepsilon,\ s - i\varepsilon;\ M^2)\big|_{i=j} = V_{NNm}(q^2)\ e^{-\alpha'_m(0)q^2\ \ln M^2} \times$$

$$\times \frac{p_\ell^2}{\pi}\frac{d\sigma^{iim}}{dtdM^2}\ (t = -q^2/4)\ e^{-2\beta'_i(0)q_T'^2\ \ln\ (s/M^2)}\ e^{-i\pi\beta_i(q_T'^2)}\ V^2_{NNi}(q_T'^2)\ , \tag{3.3}$$

where

$$\frac{d\sigma^{iim}}{dtdM^2} = (M^2)^{\alpha_m(0)-2\beta_i(q^2/4)}\ s^{2\beta_i(q^2/4)-2} \times V_{iim}(0,q^2/4,q^2/4)\ V^2_{NNi}(q^2/4)\ . \tag{3.4}$$

In the above expression $\alpha_m(t)$, $\beta_i(t)$ are the Regge trajectories and V are the triple Reggeon and Reggeon-nucleon vertex functions.

## 4. THEORY FOR DEUTERON-DEUTERON SCATTERING AT VERY HIGH ENERGIES

The theory for dd collisions is a straightforward application of Glauber theory. Also in this case one has to average the scattering operator over the two wave functions, each one in its rest system: the reference system is irrelevant, because the form factor $\hat{S}$ is relativistically invariant. The result reads [16,17]:

$$\langle\psi_1,\psi_2|\hat{F}_{dd}|\psi_1,\psi_2\rangle = 8f(q)\hat{S}^2(q/2) +$$

$$+ \frac{8i}{\pi p_\ell}\hat{S}(q/2)\int d^2q_1\ \hat{S}(q_1)f\left(\vec{q}_1 + \frac{\vec{q}}{2}\right)f\left(-\vec{q}_1 + \frac{\vec{q}}{2}\right) +$$

$$+ \frac{4i}{\pi p_\ell}\int \hat{S}^2(q_1)f\left(\vec{q}_1 + \frac{\vec{q}}{2}\right)f\left(-\vec{q}_1 + \frac{\vec{q}}{2}\right)d^2q_1 -$$

$$- \frac{8}{\pi^2 p_\ell^2}\int \hat{S}(q_1)\hat{S}(q_2)f\left(\frac{\vec{q}}{2} - \vec{q}_1\right)f(\vec{q}_1 + \vec{q}_2)f\left(\frac{\vec{q}}{2} - \vec{q}_2\right)d^2q_1d^2q_2 -$$

$$- \frac{2i}{\pi^3 p_\ell^3}\int \hat{S}(q_1)\hat{S}(q_2)f\left(\frac{\vec{q}}{2} - \vec{q}_1 - \vec{q}_3\right)f(\vec{q}_3)f(\vec{q}_1 + \vec{q}_2 + \vec{q}_3)f\left(\frac{\vec{q}}{2} - \vec{q}_2 - \vec{q}_3\right)d^2q_1d^2q_2d^2q_3\ , \tag{4.1}$$

where $q_1$, $q_2$ are the internal momentum transfers of the target and projectile deuterons. The notation is analogous to the pd case in section 3. The first term corresponds to single scattering (fig. 5a) and the next two terms to the two types of double scattering, the "normal" (fig. 5b) and the "abnormal" one (fig. 5c); the following term corresponds to triple scattering and it is depicted by the Feynman graph of fig. 5d. The last term is the quadruple scattering which is too complicated to be represented graphically; its contribution is small compared to the coherent sum of the others [17].

It is clear from the figures that only the "normal" double scattering (fig. 5b) and the triple scattering (fig. 5a) allow the modifications of the type discussed above with the inclusion of inelastic states. While for the "normal" double scattering the Gribov correction is trivially obtained from the preceding section, some care is required for the triple scattering (fig. 6).

In effect, the intermediate production of particles can occur between the first two scattering blobs [8] or between the last two. Since its analytical expression is symmetric for interchange of $q_1$ and $q_2$, one has to calculate the effect with similar techniques as for the double scattering and to multiply the result by a factor of two. The final formula reads:

$$\langle\psi_1\psi_2|\hat{F}_{dd}|\psi_1\psi_2\rangle = \hat{F}_{Glauber} + \frac{8i}{\pi p_\ell} S_0(q/2) \int d^2q_{1T}\, dM^2\, \Delta F_6^{tot}(s+i\varepsilon,\ s-i\varepsilon;\ M^2) S_0(\vec{q}_{1T}, q_{1L}) -$$

$$- \frac{16}{\pi^2 p_\ell^2} \int d^2q_{1T}\, f\left(-\vec{q}_{1T} + \frac{\vec{q}}{2}\right) S_0(q_{1T}) \int d^2q_{2T}\, dM^2\, \Delta F_6^{tot}(s+i\varepsilon, s-i\varepsilon; M^2) S_0(\vec{q}_{2T}, q_{2L}) \,. \tag{4.2}$$

The discontinuity of the six-point amplitude $\Delta F_6^{tot}$ is related to the inclusive cross-section for $pp \to pX$ through formulae (3.2) and (3.3). The arguments are the energies of the initial and final states (see fig. 4b), which are both physical, contrary to those appearing in the usual Müller diagram.

It is interesting to remark that for the Pomeron dominance $[\alpha'(0) = 0]$ one has

$$\Delta F_6^{tot}(s+i\varepsilon, s-i\varepsilon; M^2) = -e^{-(b_0/2)(q^2/4)} \frac{d\sigma}{dt dM^2} \tag{4.3}$$

and the two correction terms have different sign ($b_0$ is the slope of $d\sigma/dtdM^2$). This makes dd elastic scattering a more sensitive test of the inelastic shadow corrections to Glauber theory. Therefore, it would seem possible to test by this process also the higher order corrections studied by Kancheli and Matinyan [26].

## 5. EXPERIMENTAL RESULTS AND THEORETICAL ANALYSIS

In this section we present experimental results on pd and dd elastic scattering at both ISR energies.

The theoretical differential cross-sections, derived in the preceding paragraphs, represent absolute predictions which are directly related to the total pp cross-section in the forward direction and its slope. This allows an immediate check of the absolute normalization of the results in the region of small momentum transfers for both reactions giving confidence in the acceptance corrections applied to the data.

5.1 Proton-deuteron elastic scattering

Figure 7 shows our lower energy data points compared with Fermilab [12] and ISR [13] results on an expanded t-scale. All the available small-angle data show very good agreement with the theoretical prediction of eq. (3.2), which describes very accurately the forward differential cross-section. Our results over the entire t-range are shown in figs. 8 and 9 at both energies.

The data extend from $-t = 0.06$ GeV$^2$ to $-t = 1.65$ GeV$^2$ at $\sqrt{s} = 53$ GeV and from $-t = 0.08$ GeV$^2$ to $-t = 1.85$ GeV$^2$ at $\sqrt{s} = 63$ GeV. The statistics correspond to 178 166 and 205 600 fitted events in the two cases, with 1 754 and 5 166 events above $-t = 0.35$ GeV$^2$, respectively. The numerical results on the differential cross-sections are given in table 2. Exponential fits to the data in limited t-intervals yield approximate values of the slopes in the single and double scattering regions, about 30 GeV$^{-2}$ and 5 GeV$^{-2}$, respectively. Given the high values of the slopes in the forward direction, even more so for the dd scattering case, the effect of the experimental t-resolution modifies to a sizeable extent the t-dependence of the true cross-section. We can empirically describe the true t-dependence of the cross-sections by fitting to the data the double-exponential form

$$\frac{d\sigma}{dt} = \left| \sqrt{a_1}\, e^{(b_1/2)t} + \sqrt{a_2}\, e^{(b_2/2)t+i\phi} \right|^2 , \qquad (5.1)$$

after convolution with the experimental resolution function. The results are given in table 3.

The curves in figs. 8 and 9 are the theoretical predictions of eq. (3.2) convoluted with the experimental resolution.

The ingredients of the theoretical calculation are the following:

i) the proton-proton amplitude

$$f(q) = \frac{p_\ell}{4\pi}\,\sigma_T\left[i + \rho(t)\right] e^{bt} \qquad (5.2)$$

with

$$\rho(t) = \rho(0) + \frac{\pi}{2}\left[\alpha(t) - 1\right], \qquad (5.3)$$

where $\sigma_t$ is calculated using the parametrization of Amaldi et al. [27], $\rho(0)$ is the measured value [27], and $\alpha(t)$ is the Pomeron trajectory. This position is consistent with derivative analycity relations [28]. The slope is $2b(t) = b_0(t) + 2\alpha(t)\ \ln s/s_0$, $b_0 = 8.23\ \text{GeV}^{-2}$ and $\alpha = 0.278$ for $-t < 0.15\ \text{GeV}^2$, and $b_0 = 9.21\ \text{GeV}^{-2}$ and $\alpha = 0.10$ for $-t < 0.15\ \text{GeV}^2$ [29];

ii) the deuteron wave functions u(r) and w(r) in the analytic representation of McGee [30];

iii) the parametrization of the resonant part of the inclusive spectrum for $pp \to pX$ [31];

iv) the triple-Regge parametrizations [32-34] of the large mass $(d\sigma/dtdM)(pp \to pX)$. The slopes of $V_{ppm}$ are determined in a self-consistent way with the existing parametrizations.

It is clear from figs. 10 and 11 that in the region $0.2 \leq -t \leq 0.75\ \text{GeV}^2$ the experimental cross-section lies definitely far from the prediction of the pure Glauber theory (3.1) and that the addition of the IIS is able to explain this large discrepancy. This is particularly evident from figs. 10b and 11b, where the ratio $(d\sigma/dt)/(d\sigma/dt)_{\text{Glauber}}$ shows a beautiful interference pattern. The reason is that adding coherently the terms in eq. (3.2) causes a reduction in the single scattering region and an enhancement in the double scattering shoulder.

In fig. 11a, we also show the relative contribution of the resonant part of the $M^2$ integral in eq. (3.2), which is of the same order of magnitude as the higher mass contribution. We have assumed as separation mass between resonant and high mass regions $M_S^2 = 3.2\ \text{GeV}^2$, which is still above the second major resonance in the diffractive spectrum, since taking a higher value for $M_S^2$ the prediction is slightly above the high $|t|$ points of the angular distribution. We have used everywhere

the triple-Regge parametrization of Field and Fox [32] and neglected the quadrupole form factor in the IIS of eq. (3.2).

We have also tested the sensitivity of the pd differential cross-section to the triple Regge parametrization, plotting in fig. 12 the fractional difference

$$P = \left[\frac{d\sigma}{dt}\,(FF) - \frac{d\sigma}{dt}\,(D)\right] \Big/ \frac{d\sigma}{dt}\,(FF)\ , \qquad (5.4)$$

where FF stands for Field and Fox [32] and D for Dakhno [34]. This quantity reaches at $-t = 0.4$ GeV$^2$ a maximum value of 12%, which is much above error in the fractional difference between reference cross-section $(d\sigma/dt)/(FF)$ and experimental data. In the same figure we show the quantity P for the Roy and Roberts parametrization [33], which seems more consistent with the data than the one by Dakhno [34]. The parameters used for the three different triple-Regge fits are given in tables 4, 5, and 6. The slopes of the hadron-Reggeon form factors are fixed consistently with the Dakhno parametrization.

On the grounds of the observed agreement between theory and experimental results, we can derive from eq. (3.3) the inelastic contribution to the total cross-section defect, which is compared in fig. 13 with existing lower energy values [35]. The two ISR points show that $\delta\sigma_{inel}$ is a rapidly varying function of energy at least up to an equivalent laboratory momentum of 1000 GeV/c. We have calculated these two values using the Roy and Roberts parametrization [33], which avoids the complications connected with the explicit presence of the pion-exchange term.

In the differential cross-section a sizeable energy dependence is observed between PS and ISR energies, as shown in fig. 14 where data at 12.8 and 24.0 GeV/c are compared with our higher-energy data. This dependence, which amounts to about a factor of 10 at $-t = 2$ GeV$^2$, is mainly associated with the conspicuous shrinkage of the elastic pp cross-section over the same energy range.

5.2 Deuteron-deuteron elastic scattering

The experimental results on the dd differential cross-sections at $\sqrt{s} = 53$ and $\sqrt{s} = 63$ GeV are shown in figs. 15 and 16.

The data at $\sqrt{s}$ = 53 GeV extend from $-t = 0.06$ GeV$^2$ to 1.4 GeV$^2$ and at $\sqrt{s}$ = 63 GeV from $-t = 0.08$ GeV$^2$ to 1.41 GeV$^2$. The statistics correspond to 57 443 and 75 328 fitted events in the two cases, with 1 925 and 5 819 events above $-t = 0.18$ GeV$^2$, respectively. The numerical results are given in table 7.

Contrary to the pd case, a narrow interference minimum is clearly present at both energies. The exponential slopes below and above the interference region are about 56 GeV$^{-2}$ and 6.5 GeV$^{-2}$, respectively. Also in this case an empirical fit with two interfering exponentials can give a good description of the t-dependence of the true differential cross-section. Given the very high value of the first slope, this is sensibly modified by the finite t-resolution of the experiment. The parameters describing the deconvoluted differential cross-sections, according to eq. (5.1), are given in table 8.

From these fits true values for the position of the minimum and for the corresponding differential cross-section are found to be

$$-t_{min} = (0.179 \pm 0.005)\ \text{GeV}^2,\ d\sigma/dt_{min} = (37.28 \pm 7.86)\ \mu\text{b/GeV}^2, \quad \text{at } \sqrt{s} = 53\ \text{GeV}$$

$$-t_{min} = (0.183 \pm 0.005)\ \text{GeV}^2,\ d\sigma/dt_{min} = (33.78 \pm 8.57)\ \mu\text{b/GeV}^2, \quad \text{at } \sqrt{s} = 63\ \text{GeV} \qquad (5.5)$$

The curves in figs. 15 and 16 are the theoretical predictions of eq. (4.2) after convolution with the experimental t-resolution.

The ingredients in the calculation are the same as for the pd case.

Also in the dd case there is an apparent discrepancy between experimental data and predictions of Glauber theory [17], as shown in figs. 17 and 18. With the coherent sum of the inelastic corrections to the "normal" double scattering and to the triple scattering one recovers the agreement. From figs. 17a and 18a, where the results including only the correction to the triple scattering are plotted, it is clear that this is the result of a delicate cancellation between the two terms of eq. (4.2): for these reasons dd elastic scattering provides a very sensitive test of the theory.

This cancellation is also visible in fig. 19, where we plot the fractional difference in the spin-independent amplitude $F_1$ of Ref. 17

$$F = (F_1^{IIS} - F_1^C)/F_1^G \ , \qquad (5.6)$$

where IIS stands for inelastic intermediate states and G for Glauber. The solid line is obtained by considering both terms of eq. (4.2), the dashed line only the second correction term, and the dotted line only the first one.

It is clear that after the singularity at $-t = 0.2$ GeV$^2$ the solid line results from the cancellation of the two terms. The singularity is responsible for the minimum, which is partially filled by the other spin-dependent terms [17].

In this case the sensitivity to the triple-Regge parametrization is enhanced by the cancellation, as shown in Fig. 20, in which the quantity P of eq. (5.4) for the dd case is displayed. The maximum difference is obtained again for the Dakhno parametrization [35], reaching 40% at $-t = 0.23$ GeV$^2$: the difference for Roy and Roberts [34] is small, as for the pd case*). We stress that the sensitivity of the results to the different triple-Regge parametrizations does not depend crucially on the choice of the separation mass $M_S^2$ introduced in section 5.1. For the more usual value $M_S^2 = 4$ GeV$^2$, the sensitivity is still present, although reduced. The upper limit on the $M^2$ integration was fixed in all cases requiring the convergence of the integral.

Also the dd differential cross-section, similarly to the pd case, shows a sizeable energy dependence associated with the shrinkage of the elementary pp amplitude. In fig. 21 the data at 7.9 GeV/c are compared with the results at the highest ISR energy.

The data in the high-t region differ by as much as a factor of ten, but seem to extrapolate to the same cross-section value at $t = 0$, as could be expected from a shrinkage effect. A similar consideration holds also for the pd differential cross-section in the double scattering region.

---

*) As for the pd case we did not include the quadrupole corrections in the intermediate inelastic states. Work to include the quadrupole form factor in the calculation of the integrals in eqs. (3.2) and (4.2) is in progress.

## 6. CONCLUSIONS

We have measured the pd and dd elastic differential cross-sections at the two highest ISR energies of 53 and 63 GeV c.m.s. The data extend from about $-t = 0.07$ GeV$^2$ to about $-t = 2$ GeV$^2$, covering extensively the single and multiple scattering regions. We find that around the interference region the pure Glauber theory is inadequate to describe the detailed properties of the differential cross-sections by factors as big as 30% in particular regions of t. In both cases a very good agreement between theory and experimental data can be reached by including in the basic theory corrections arising from the propagation of inelastic states in the deuteron. These corrections are generated by the virtual production of low and high masses and show an enhanced sensitivity to the form of the triple Regge parametrization describing the high mass portion of the inclusive proton excitation spectrum.

The study of these energy-dependent corrections to pd and dd multiple scattering may therefore open up a new approach to test detailed mechanisms of the elementary pp interaction.

Acknowledgements

We thank the PS and ISR Divisions for their efforts in realizing the acceleration and storage of deuterons. The excellent support of the SFM detector and data-handling groups is also gratefully acknowledged. We thank A. Brandt, F. Niebergall and J. Schuett for their contributions which were essential to the success of this work. We thank L. Bertocchi for useful discussions.

REFERENCES

[1] H.C. Hsiung et al., Phys. Rev. Letters 21 (1968) 187.
M. Fellinger et al., Phys. Rev. Letters 22 (1964) 1265.
F. Bradamante et al., Nuclear Phys. B33 (1971) 165.

[2] E. Coleman et al., Phys. Rev. 164 (1967) 1655.
G.W. Bennet et al., Phys. Rev. Letters 19 (1967) 387.
F. Bradamante et al., Phys. Letters B32 (1976) 303.
J.V. Allaby et al., Phys. Letters B30 (1969) 500.

[3] R.J. Glauber in Lectures in Theoretical Physics (Ed. W.E. Brittin et al.) (Interscience, NY., 1959), Vol. 1, p. 315.

[4] R.J. Glauber and V. Franco, Phys. Rev. 156 (1967) 1685.

[5] C.J. Joachain and C. Quigg, Rev. Mod. Phys. 46 (1974) 279.

[6] C. Michael and C. Wilkin, Nuclear Phys. B11 (1969) 99.
V. Franco and R.J. Glauber, Phys. Rev. Letters 22 (1969) 370.
G. Alberi and L. Bertocchi, Nuovo Cimento 63A (1969) 285.

[7] F. Bradamante et al., Phys. Letters B31 (1970) 87.

[8] G. Fäldt, Nuclear Phys. B29 (1971) 16.
J.F. Gunion and R. Blankenbecler, Phys. Rev. D 3 (1971) 2125.
J.M. Namyslowski, Nuovo Cimento Letters 5 (1972) 999.

[9] J. Harter and D.I. Julius, Nuclear Phys. B116 (1974) 400.

[10] N. Zovko, Nuclear Phys. B91 (1975) 517.

[11] U. Amaldi et al., Nuclear Phys. B39 (1972) 1.

[12] Y. Akimov et al., Phys. Rev. D 12 (1975) 3399.

[13] J.C.M. Armitage et al., Nuclear Phys. B132 (1978) 365.

[14] A.T. Goshaw et al., Phys. Rev. Letters 23 (1969) 990.

[15] A.T. Goshaw et al., Phys. Rev. Letters 25 (1970) 249.

[16] V. Franco, Phys. Rev. 175 (1968) 1376.

[17] G. Alberi et al., Nuclear Phys. B17 (1970) 621.

[18] G. Alberi and F. Baldracchini, Preprint CERN TH 2443, to be published in Nuclear Phys. B and references contained therein.

[19] G. Goggi et al., Evidence for inelastic propagators in proton-deuteron elastic scattering at $\sqrt{s}$ = 63 GeV, Phys. Letters B, in press; Observation of a narrow minimum and of inelastic shadow effects in deuteron-deuteron elastic scattering at $\sqrt{s}$ = 53 GeV, Phys. Letters B, in press.

[20] R. Bouclier et al., Nuclear Instrum. Methods 115 (1974) 235.

[21] L. Bertocchi and A. Capella, Nuovo Cimento 51A (1967) 369.

[22] E.S. Abers et al., Nuovo Cimento 42A (1966) 363.

[23] V.N. Gribov, Zh. Eksper. Teor. Fiz. 56 (1960) 892. [English transl.: Soviet Phys. JETP 29 (1965) 483.]

[24] O.V. Kancheli and S.G. Matinyan, Zh. Eksper. Teor. Fiz. Pis'ma 12 (1970) 41. [English transl.: JETP Letters 12 (1970) 30.]

C. Quigg and L.L. Wang, Phys. Letters 43B (1973) 314.

[25] J. Kwiecinski et al., Nuclear Phys. B78 (1974) 251.

[26] O.V. Kancheli and S.V. Matinyan, Yadernaya Fiz. 13 (1971) 143. [English transl.: Sov. J. Nuclear Phys. 13 (1971) 82.]

[27] U. Amaldi et al., Phys. Letters 66B (1977) 390.

[28] J.B. Bronzan et al., Phys. Letters 49B (1974) 272.

[29] G. Giacomelli, Phys. Reports 23C (1976) 123, especially p. 182.

[30] J.I. McGee, Phys. Rev. 151 (1966) 772.

[31] G. Hendrick et al., Phys. Rev. D 11 (1975) 536.

[32] R.D. Field and G.C. Fox, Nuclear Phys. B80 (1974) 367.

[33] D.P. Roy and R.G. Roberts, Nuclear Phys. B77 (1974) 240.

[34] L.G. Dakhno, Yadernaya Fiz. 23 (1976) 862. [English transl.: Sov. J. Nuclear Phys. 23 (1976) 454.]

[35] L.G. Dakhno, IFVE, 76-117, Serpukhov 1976, and references contained therein.

Table 1

Parameters of the pd and dd data samples

| | Reaction | $p_{lab}$ (GeV/c) | $\int \mathscr{L}\, dt$ ($\mu b^{-1}$) | Events | Systematic uncertainty (%) |
|---|---|---|---|---|---|
| $\sqrt{s}$ = 53 GeV | pd ← pd | 737 | 6 744 | 178 166 | 5 |
| | dd → dd | 740 | 3 292 | 57 443 | 5 |
| $\sqrt{s}$ = 63 GeV | pd → pd | 1 034 | 14 443 | 205 600 | 9 |
| | dd → dd | 1 037 | 9 204 | 75 328 | 9 |

Table 2

Differential cross-sections for pd elastic scattering

| $\sqrt{s}$ = 53 GeV | | | $\sqrt{s}$ = 63 GeV | | |
|---|---|---|---|---|---|
| $-t$ ($GeV^2$) | $d\sigma/dt$ ($\mu b/GeV^2$) | $\Delta(d\sigma/dt)$ ($\mu b/GeV^2$) | $-t$ ($GeV^2$) | $d\sigma/dt$ ($\mu b/GeV^2$) | $\Delta(d\sigma/dt)$ ($\mu b/GeV^2$) |
| 0.06 | 33 865.0 | 2 391.0 | 0.08 | 17 524.0 | 1 266.0 |
| 0.08 | 17 567.0 | 1 075.0 | 0.10 | 8 984.0 | 582.0 |
| 0.10 | 10 374.0 | 570.0 | 0.12 | 5 215.0 | 309.0 |
| 0.12 | 5 610.0 | 284.0 | 0.14 | 3 182.0 | 175.0 |
| 0.14 | 2 900.0 | 139.0 | 0.16 | 1 782.0 | 93.0 |
| 0.16 | 1 686.0 | 78.0 | 0.18 | 1 013.0 | 51.0 |
| 0.18 | 931.3 | 41.7 | 0.20 | 570.4 | 28.4 |
| 0.20 | 571.8 | 25.1 | 0.23 | 271.8 | 12.9 |
| 0.23 | 306.9 | 12.5 | 0.27 | 109.5 | 5.1 |
| 0.27 | 108.1 | 6.2 | 0.31 | 52.66 | 2.53 |
| 0.31 | 59.71 | 4.08 | 0.35 | 39.38 | 1.91 |
| 0.35 | 40.56 | 2.97 | 0.39 | 37.83 | 1.94 |
| 0.39 | 35.45 | 2.91 | 0.43 | 33.03 | 1.93 |
| 0.43 | 35.98 | 3.10 | 0.47 | 26.25 | 1.70 |
| 0.47 | 26.62 | 2.45 | 0.51 | 21.95 | 1.55 |
| 0.51 | 24.68 | 2.86 | 0.55 | 20.71 | 1.42 |
| 0.55 | 19.45 | 2.48 | 0.59 | 17.43 | 1.11 |
| 0.59 | 17.29 | 2.34 | 0.63 | 13.66 | 1.30 |
| 0.63 | 13.71 | 1.89 | 0.67 | 10.62 | 1.19 |
| 0.67 | 11.57 | 1.74 | 0.71 | 9.71 | 1.17 |
| 0.71 | 9.77 | 1.49 | 0.75 | 7.94 | 1.06 |
| 0.75 | 8.60 | 1.64 | 0.79 | 6.61 | 1.03 |
| 0.79 | 6.81 | 1.39 | 0.83 | 4.85 | 0.84 |
| 0.83 | 6.02 | 1.35 | 0.89 | 3.56 | 0.49 |
| 0.89 | 3.53 | 0.72 | 0.97 | 2.48 | 0.43 |
| 0.97 | 2.20 | 0.55 | 1.05 | 1.27 | 0.30 |
| 1.05 | 1.91 | 0.52 | 1.13 | 0.91 | 0.25 |
| 1.17 | 0.80 | 0.24 | 1.21 | 0.80 | 0.37 |
| 1.37 | 0.30 | 0.12 | 1.29 | 0.47 | 0.18 |
| 1.65 | 0.11 | 0.04 | 1.41 | 0.23 | 0.08 |
| | | | 1.61 | 0.08 | 0.04 |
| | | | 1.85 | 0.02 | 0.01 |

Table 3

Parameters describing the deconvoluted elastic pd cross-section [eq. (5.1)]

| | $\sqrt{s}$ = 53 GeV | $\sqrt{s}$ = 63 GeV |
|---|---|---|
| $a_1$ (mb/GeV$^2$) | 172.63 ± 4.94 | 141.15 ± 11.08 |
| $b_1$ (GeV$^{-2}$) | 28.29 ± 0.11 | 25.81 ± 0.75 |
| $a_2$ (mb/GeV$^2$) | 0.275 ± 0.025 | 0.392 ± 0.059 |
| $b_2$ (GeV$^{-2}$) | 4.81 ± 0.14 | 5.38 ± 0.21 |
| $\phi$ (rad) | 1.94 ± 0.03 | 2.19 ± 0.07 |
| $\chi^2$/d.f. | 1.27 | 0.94 |

Table 4

Parameters[a] of the triple-Regge expansion of Field and Fox [32]

| | $\mathbb{P}\mathbb{P}\mathbb{P}$ | $\mathbb{P}MM$ | $M\mathbb{P}\mathbb{P}$ | $MMM$ | $\mathbb{P}\pi\pi$ | $M\pi\pi$ |
|---|---|---|---|---|---|---|
| $V_1$ [mb/(GeV)$^4$] | 6.26 | 24.64 | 0.71 | 18.7 | -73.73 | -68.19 |
| $V_2$ [mb/(GeV)$^4$] | 38.6 | 2.8 | 6.49 | 0 | 0 | 0 |
| $\beta_1$ [GeV$^{-2}$] | 3.69 | 8.3 | -0.62 | 12.00 | 0 | 0 |
| $\beta_2$ [GeV$^{-2}$] | 10.1 | -2.0 | 6.5 | 0 | 0 | 0 |
| $\beta_i(0)$ | 1.0 | 0.5 | 1.0 | 0.5 | 0 | 0 |
| $\beta_i'(0)$ [GeV$^{-2}$] | 0.39 | 1.0 | 0.39 | 1.0 | 1.0 | 1.0 |
| $\alpha_m(0)$ | 1.0 | 1.0 | 0.5 | 0.5 | 1.0 | 0.5 |
| $\alpha_m'(0)$ [GeV$^{-2}$] | 0.39 | 0.39 | 1.0 | 1.0 | 0.39 | 1.0 |
| $\beta_{pmm}$ [GeV$^{-2}$] | 3.38 | 3.38 | 4.81 | 4.81 | 3.38 | 4.81 |
| $\eta_i$ | 1.0 | 1.0 | 1.0 | 1.0 | 1.0 | 1.0 |

a) The notation is the same as in eqs. (3.3) and (3.4). The first four parameters give the behaviour of the vertex function $V_{iim}V^2_{NNi} = V_1\, e^{\beta_1 t} + V_2\, e^{\beta_2 t}$.

Table 5

Parameters of the triple-Regge expansion of Roy and Roberts [33]

| | PPP | MPP | PMM | MMM |
|---|---|---|---|---|
| $V_1$ [mb/(GeV)$^4$] | 6.0 | 5.5 | 180.0 | 400.0 |
| $V_2$ [mb/(GeV)$^4$] | 2.0 | -5.5 | -160.0 | 100.0 |
| $\beta_1$ [GeV$^{-2}$] | 18.0 | 4.0 | 3.5 | 18.0 |
| $\beta_2$ [GeV$^{-2}$] | 3.0 | 9.0 | 20.0 | 3.0 |
| $\beta_i(0)$ | 1.0 | 1.0 | 0.2 | 0.2 |
| $\beta_i'(0)$ [GeV$^{-2}$] | 0.25 | 0.25 | 0.5 | 0.5 |
| $\alpha_m(0)$ | 1.0 | 0.2 | 1.0 | 0.2 |
| $\alpha_m'(0)$ [GeV$^{-2}$] | 0.25 | 0.5 | 0.25 | 0.5 |
| $\beta_{pmm}$ [GeV$^{-2}$] | 3.38 | 2.0 | 3.38 | 2.0 |
| $\eta_i$ | 1.0 | 1.0 | 1.0 | 1.0 |

Table 6

Parameters of the triple-Regge expansion of Dakhno [34]

| | $\mathbb{P}\mathbb{P}\mathbb{P}$ | $\mathbb{P}\pi\pi$ | $\mathbb{P}\mathbb{P}''\mathbb{P}''$ | $M\mathbb{P}\mathbb{P}$ | MMM | $S\mathbb{P}\mathbb{P}$ | SMM | $S\mathbb{P}''\mathbb{P}''$ |
|---|---|---|---|---|---|---|---|---|
| $V_1$ [mb/(GeV)$^4$] | 27.6 | -179.04 | 186.0 | 114.0 | -1260.0 | -234.0 | 2446.0 | 1861.0 |
| $V_2$ [mb/(GeV)$^4$] | 0 | 0 | 0 | 0 | 0 | 0 | 0 | 0 |
| $\beta_1$ [GeV$^{-2}$] | 6.76 | 3.3 | 6.76 | 12.96 | 9.61 | 13.69 | 9.61 | 5.29 |
| $\beta_2$ [GeV$^{-2}$] | 0 | 0 | 0 | 0 | 0 | 0 | 0 | 0 |
| $\beta_i(0)$ | 1.0 | 0 | 0 | 1.0 | 0.5 | 1.0 | 0.5 | 0 |
| $\beta_i'(0)$ [GeV$^{-2}$] | 0.28 | 1.0 | 0 | 0.28 | 1.0 | 0.28 | 1.0 | 0 |
| $\alpha_m(0)$ | 1.0 | 1.0 | 1.0 | 0.5 | 0.5 | 0 | 0 | 0 |
| $\alpha_m'(0)$ [GeV$^{-2}$] | 0.28 | 0.28 | 0.28 | 1.0 | 1.0 | 0 | 0 | 0 |
| $\beta_{pmm}$ [GeV$^{-2}$] | 3.38 | 3.38 | 3.38 | 4.81 | 4.81 | 3.38 | 3.38 | 3.38 |
| $\eta_i$ | 1.0 | 1.0 | 1.0 | 1.0 | 1.0 | 1.0 | 1.0 | 1.0 |

Table 7

Differential cross-sections for dd elastic scattering

| $\sqrt{s}$ = 53 GeV | | | $\sqrt{s}$ = 63 GeV | | |
|---|---|---|---|---|---|
| $-t$ ($GeV^2$) | $d\sigma/dt$ ($\mu b/GeV^2$) | $\Delta(d\sigma/dt)$ ($\mu b/GeV^2$) | $-t$ ($GeV^2$) | $d\sigma/dt$ ($\mu b/GeV^2$) | $\Delta(d\sigma/dt)$ ($\mu b/GeV^2$) |
| 0.06 | 22 505.0 | 1 662.0 | 0.08 | 7 740.0 | 560.0 |
| 0.08 | 7 382.0 | 516.0 | 0.10 | 2 398.0 | 156.0 |
| 0.10 | 2 585.0 | 146.0 | 0.12 | 895.8 | 54.1 |
| 0.12 | 794.9 | 44.2 | 0.14 | 278.0 | 16.4 |
| 0.14 | 234.5 | 15.8 | 0.16 | 86.61 | 5.62 |
| 0.16 | 94.03 | 8.61 | 0.18 | 40.40 | 3.08 |
| 0.18 | 47.15 | 4.93 | 0.20 | 41.36 | 3.26 |
| 0.20 | 41.14 | 4.16 | 0.23 | 51.94 | 3.17 |
| 0.22 | 47.29 | 4.21 | 0.27 | 57.24 | 2.95 |
| 0.24 | 55.89 | 4.48 | 0.31 | 48.73 | 2.40 |
| 0.27 | 55.13 | 3.40 | 0.35 | 41.46 | 1.99 |
| 0.31 | 54.12 | 3.73 | 0.39 | 33.80 | 1.76 |
| 0.35 | 40.56 | 3.43 | 0.43 | 23.37 | 1.49 |
| 0.39 | 36.60 | 3.49 | 0.47 | 15.64 | 1.25 |
| 0.43 | 21.46 | 2.59 | 0.51 | 14.22 | 1.23 |
| 0.47 | 14.82 | 2.19 | 0.55 | 9.23 | 1.00 |
| 0.51 | 11.03 | 1.92 | 0.59 | 8.24 | 1.00 |
| 0.55 | 8.70 | 1.72 | 0.65 | 5.27 | 0.57 |
| 0.59 | 5.24 | 1.25 | 0.73 | 3.00 | 0.44 |
| 0.65 | 4.82 | 0.91 | 0.81 | 1.21 | 0.28 |
| 0.73 | 3.01 | 0.68 | 0.89 | 0.92 | 0.24 |
| 0.81 | 1.88 | 0.57 | 0.97 | 0.60 | 0.19 |
| 0.89 | 0.80 | 0.37 | 1.05 | 0.39 | 0.10 |
| 0.97 | 0.84 | 0.38 | 1.13 | 0.20 | 0.07 |
| 1.09 | 0.36 | 0.16 | 1.21 | 0.13 | 0.05 |
| 1.25 | 0.20 | 0.12 | 1.41 | 0.03 | 0.02 |
| 1.40 | 0.07 | 0.07 | | | |

Table 8

Parameters describing the deconvoluted elastic dd cross-section [eq. (5.1)]

| | $\sqrt{s}$ = 53 GeV | $\sqrt{s}$ = 63 GeV |
|---|---|---|
| $a_1$ (mb/GeV$^2$) | 416.23 ± 44.84 | 240.80 ± 61.38 |
| $b_1$ (GeV$^{-2}$) | 47.73 ± 1.29 | 44.84 ± 1.79 |
| $a_2$ (mb/GeV$^2$) | 0.471 ± 0.057 | 0.532 ± 0.061 |
| $b_2$ (GeV$^{-2}$) | 7.08 ± 0.28 | 7.2 ± 0.23 |
| $\phi$ (rad) | 2.59 ± 0.04 | 2.64 ± 0.03 |
| $\chi^2$/d.f. | 1.12 | 0.76 |

Figure captions

Fig. 1 : Plan view of the SFM detector, showing the layout of the magnetic structure and of the multiwire proportional chambers.

Fig. 2 : Correlation between measured final state momenta in the two spectrometer arms at $\sqrt{s}$ = 53 GeV in:

a) pd collisions;

b) dd collisions.

Elastic scattering appears clearly separated from single and double break-up processes. Different peak heights arise from an interplay of trigger acceptance and deuteron form factors.

Fig. 3 : Feynman graph representation of the pd elastic scattering amplitudes for:

a) single scattering;

b) double scattering.

Fig. 4 : Inelastic corrections to the double scattering diagram:

a) inelastic intermediate states in double scattering;

b) explicit Reggeon representation of inelastic amplitudes;

c) triple-Regge representation of (a).

Fig. 5 : Feynman graph representation of the dd elastic scattering amplitude:

a) single scattering;

b) "normal" double scattering;

c) "abnormal" double scattering;

d) triple scattering.

Fig. 6 : Inelastic correction to the triple scattering.

Fig. 7 : Comparison of high-energy differential cross-sections for pd elastic scattering in the low-t region. The solid curve is the prediction of the extended Glauber theory, eq. (4.2).

Fig. 8 : Differential cross-section for pd elastic scattering at $\sqrt{s}$ = 53 GeV. The solid curve is the absolute prediction of the full theory.

Fig. 9 : Differential cross-section for pd elastic scattering at $\sqrt{s}$ = 63 GeV. The solid curve is the absolute prediction of the full theory.

Fig. 10 : a) Differential cross-section for pd elastic scattering at $\sqrt{s}$ = 53 GeV on an expanded t-scale around the interference region. The dashed line is the pure Glauber theory.

b) Ratio of both full theory and experimental data to the Glauber prediction as a function of t at $\sqrt{s}$ = 53 GeV.

Fig. 11 : a) Differential cross-section for pd elastic scattering at $\sqrt{s}$ = 63 GeV on an expanded t-scale, around the interference region. The dashed line is the pure Glauber theory; the dotted line shows the contribution of only resonance states to the inelastic propagators.

b) Ratio of data and full theory to pure Glauber theory at $\sqrt{s}$ = 63 GeV.

Fig. 12 : t-dependence of the fractional difference P [eq. (5.4)] between different Regge parametrizations as input to the full theory for pd scattering (see text). The reference parametrization is taken to be the one of Field and Fox [32].

Fig. 13 : Inelastic contribution to the pd total cross-section defect as a function of equivalent laboratory momentum. Data up to 300 GeV/c are taken from Ref. 35. The errors in the ISR points represent the uncertainty on the triple-Regge parameters used in the calculation.

Fig. 14 : Comparison of pd elastic differential cross-sections at low energies and at the highest ISR energy. Data at 12.8 GeV/c and 24 GeV/c are from Bradamante et al. [2] and Amaldi et al. [11].

Fig. 15 : Differential cross-section for dd elastic scattering at $\sqrt{s}$ = 53 GeV. The solid curve is the absolute prediction of the full theory.

Fig. 16 : Differential cross-section for dd elastic scattering at $\sqrt{s}$ = 63 GeV. The solid curve is the absolute prediction of the full theory.

Fig. 17 : a) Differential cross-section for dd elastic scattering at $\sqrt{s}$ = 53 GeV on an expanded t-scale around the interference region. The dashed line is the pure Glauber theory. The dashed-dotted line shows the effect of IIS in the triple scattering only.

b) Ratio of both experimental points and full theory to the Glauber term as a function of four-momentum transfer at $\sqrt{s}$ = 53 GeV.

Fig. 18 : a) Differential cross-section for dd elastic scattering at $\sqrt{s}$ = 63 GeV on an expanded t-scale around the interference region. The contributions of the pure Glauber term and of IIS in the triple scattering term are shown.

b) Ratio of both experimental points and full theory to the Glauber term as a function of four-momentum transfer at $\sqrt{s}$ = 63 GeV.

Fig. 19 : t-dependence of the quantity F [eq. (5.6)], the fractional effect of IIS on the spin-independent amplitude in dd scattering. The dashed curve is for the inclusion of IIS only in triple scattering and the dotted curve only in double scattering. The solid line is the full result and shows the partial cancellation between the two contributions.

Fig. 20 : t-dependence of the fractional difference P [eq. (5.4)] between different Regge parametrizations as input to the full theory for dd scattering (see text). The reference parametrization is taken to be that of Field and Fox [32].

Fig. 21 : Comparison of dd elastic differential cross-sections at $p_{lab}$ = 7.9 GeV/c [15] and at the highest ISR energy.

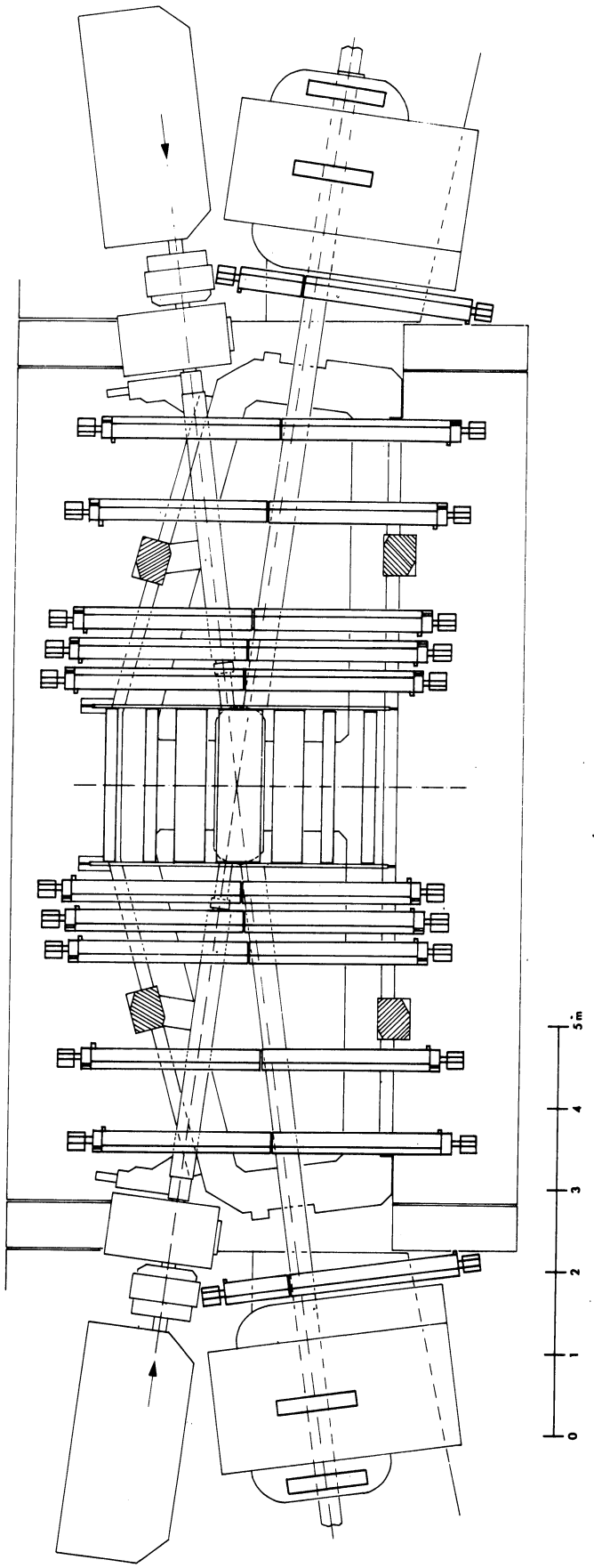


Fig. 1

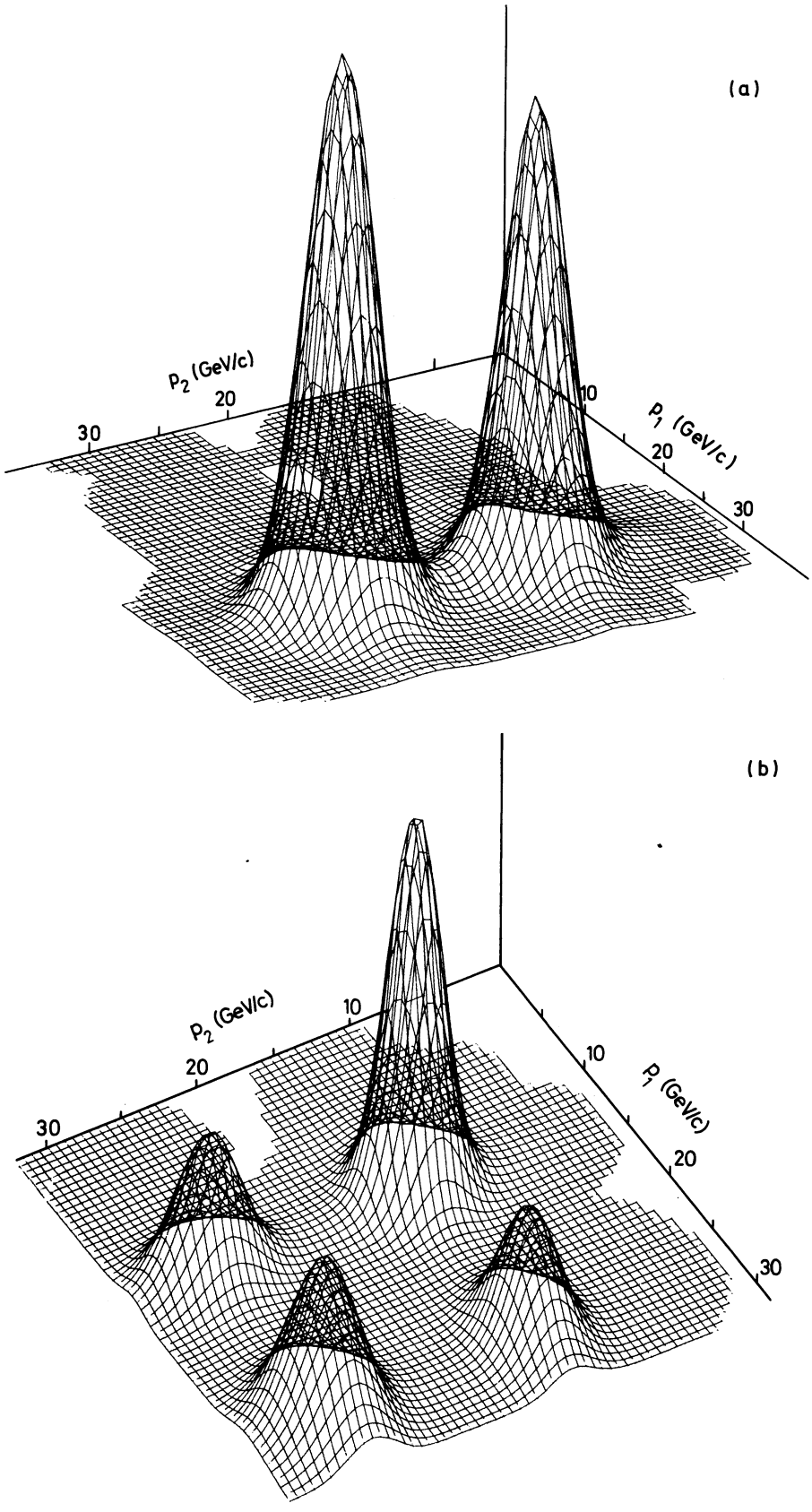


Fig. 2

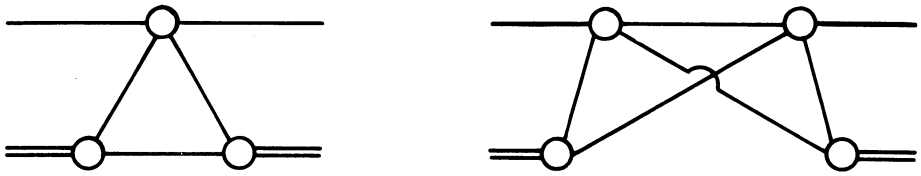

a) b)

Fig. 3

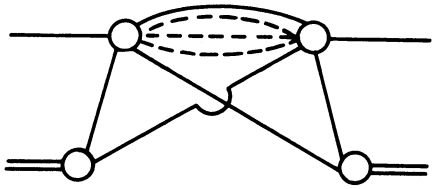

a)


b) c)

Fig. 4

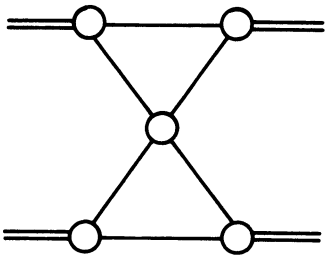

a)

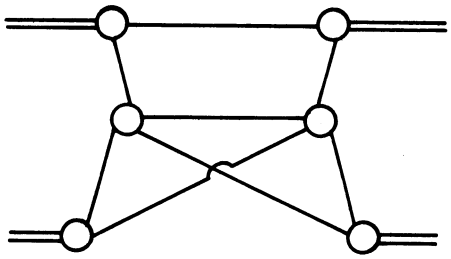

b)

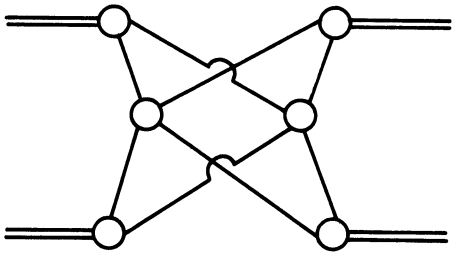

c)

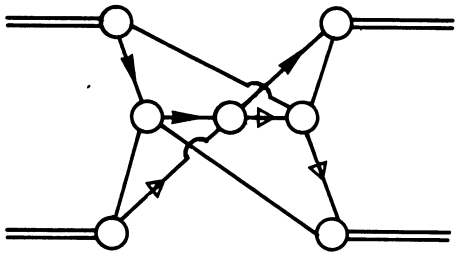

d)

Fig. 5

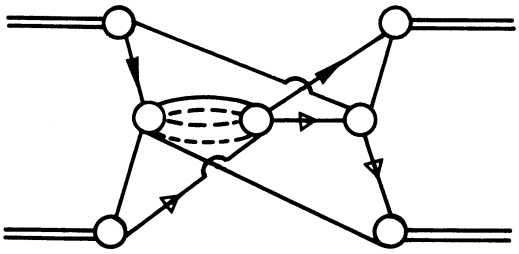

Fig. 6

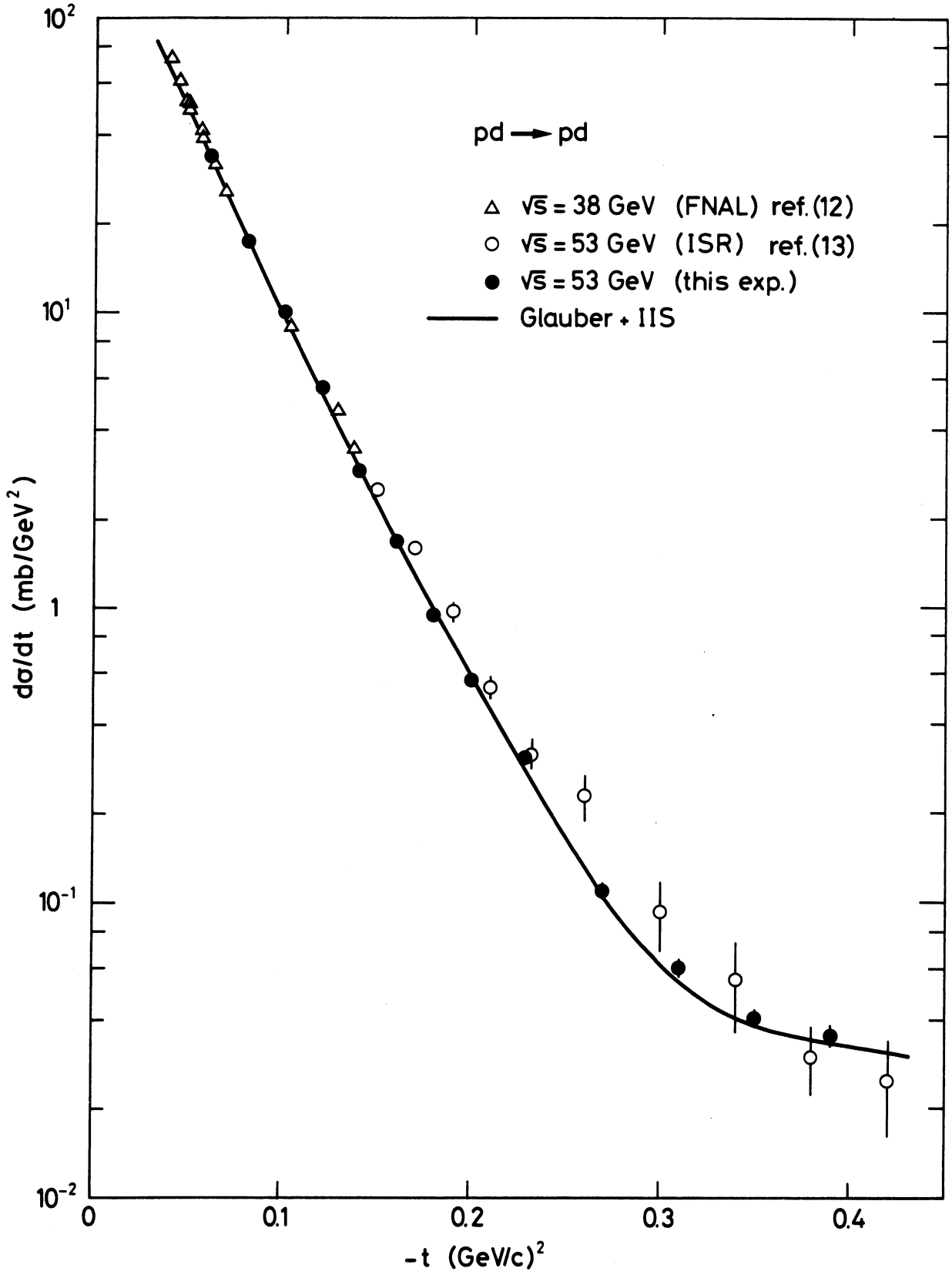
pd → pd
△ √s = 38 GeV (FNAL) ref.(12)
○ √s = 53 GeV (ISR) ref.(13)
● √s = 53 GeV (this exp.)
Glauber + IIS
dσ/dt (mb/GeV²)
-t (GeV/c)²
10²
10¹
1
10⁻¹
10⁻²
0
0.1
0.2
0.3
0.4

Fig. 7

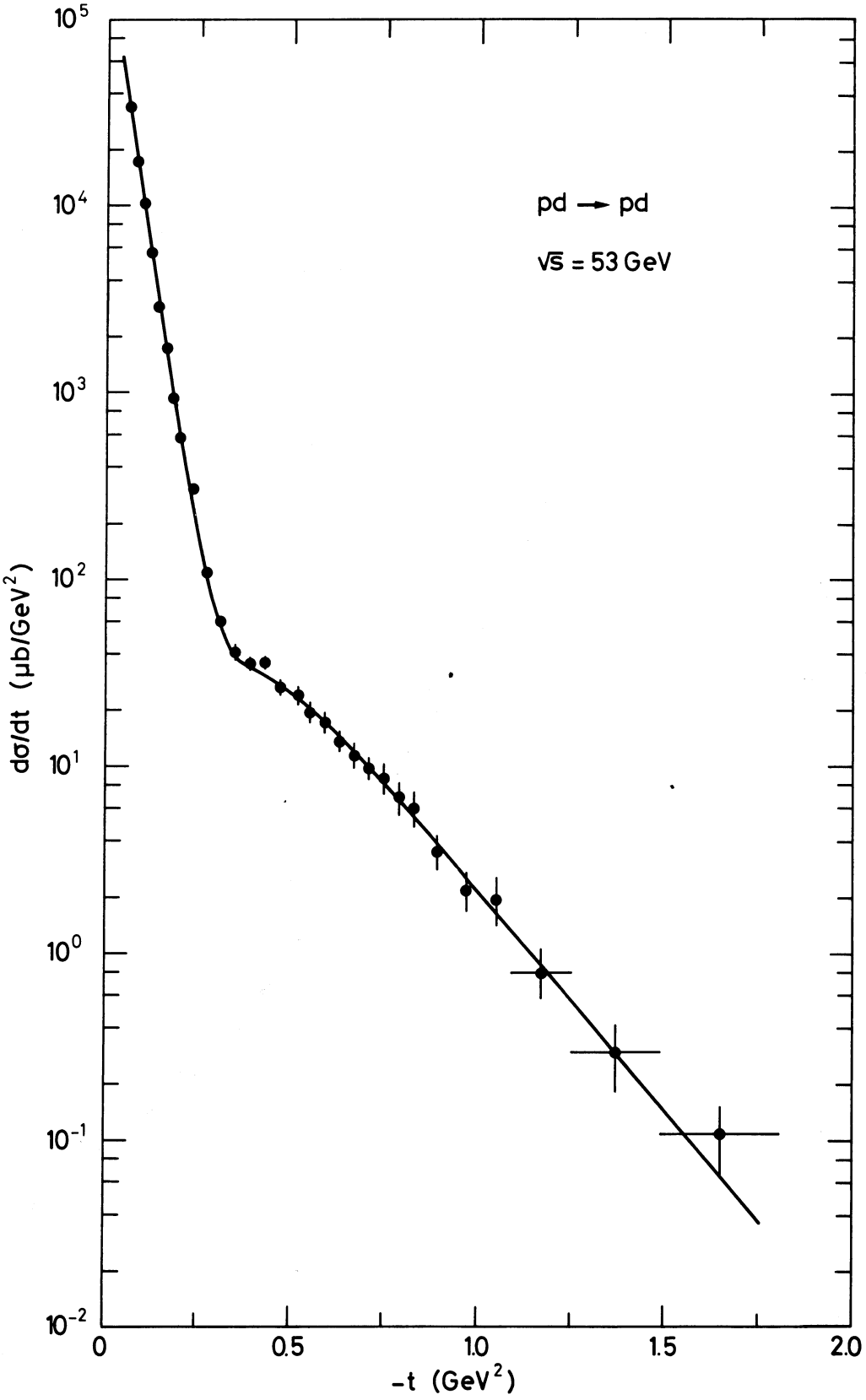
pd → pd
√s = 53 GeV
dσ/dt (μb/GeV²)
-t (GeV²)
10⁵
10⁴
10³
10²
10¹
10⁰
10⁻¹
10⁻²
0
0.5
1.0
1.5
2.0

Fig. 8

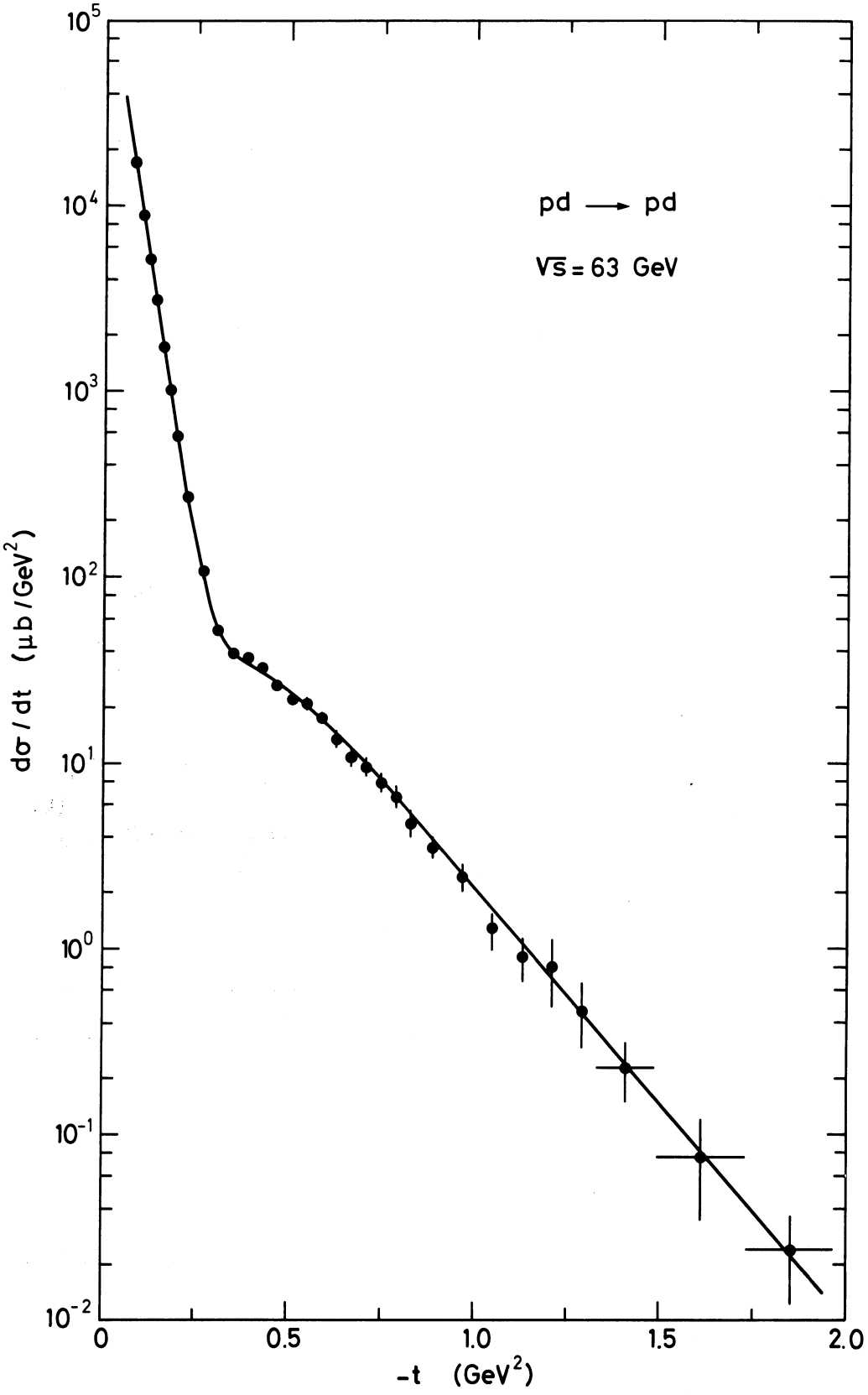
pd → pd
√s = 63 GeV
dσ / dt (μb / GeV²)
-t (GeV²)
10⁵
10⁴
10³
10²
10¹
10⁰
10⁻¹
10⁻²
0
0.5
1.0
1.5
2.0

Fig. 9

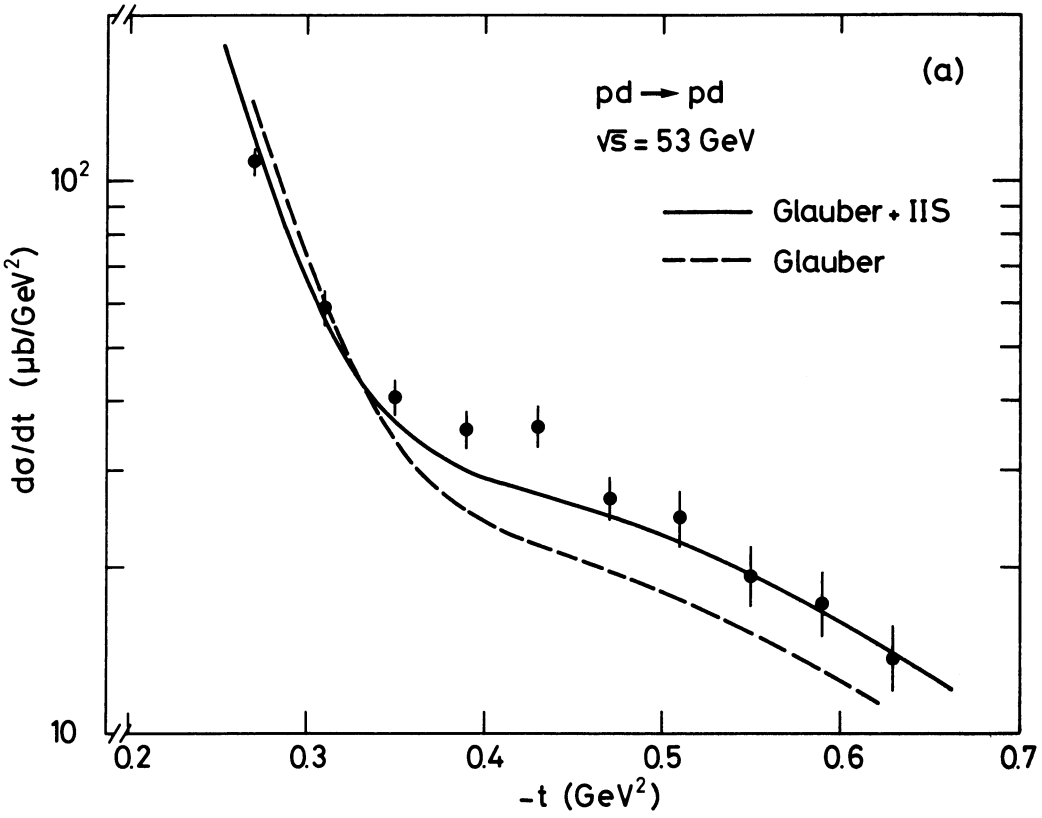
(a)
pd → pd
√s = 53 GeV
Glauber + IIS
Glauber
dσ/dt (μb/GeV²)
10²
10
0.2
0.3
0.4
0.5
0.6
0.7
-t (GeV²)

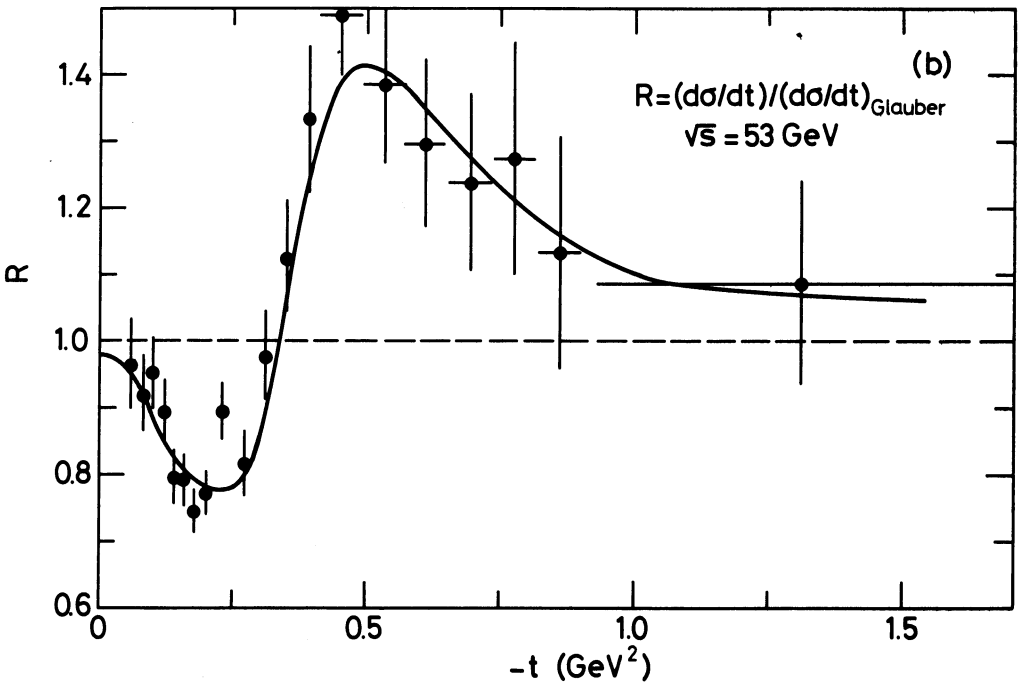
(b)
R=(dσ/dt)/(dσ/dt)Glauber
√s = 53 GeV
R
1.4
1.2
1.0
0.8
0.6
0
0.5
1.0
1.5
-t (GeV²)

Fig. 10

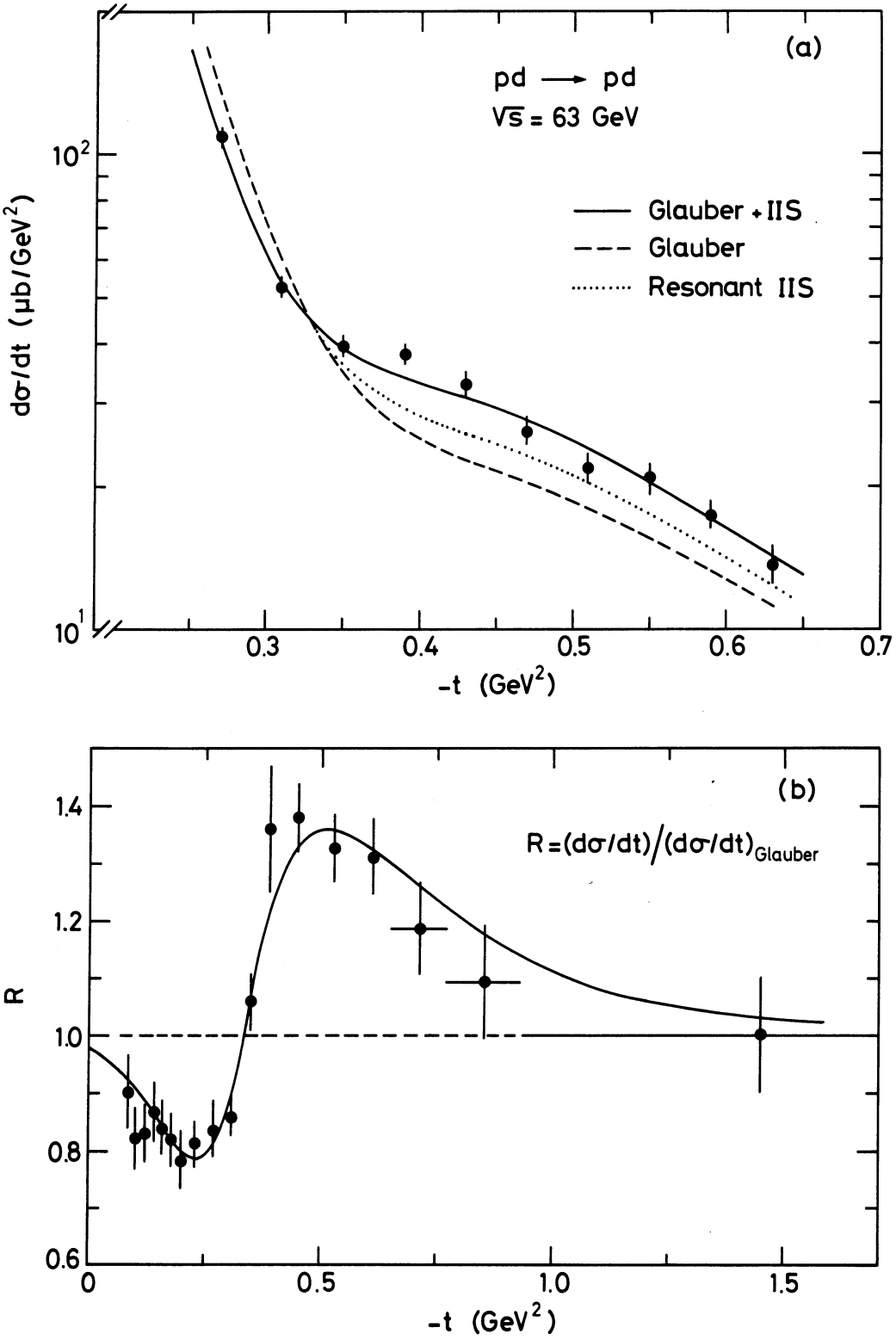
(a)
pd → pd
√s = 63 GeV
Glauber + IIS
Glauber
Resonant IIS
dσ/dt (μb/GeV²)
10²
10¹
0.3
0.4
0.5
0.6
0.7
-t (GeV²)
(b)
R = (dσ/dt)/(dσ/dt)Glauber
R
1.4
1.2
1.0
0.8
0.6
0
0.5
1.0
1.5
-t (GeV²)

Fig. 11

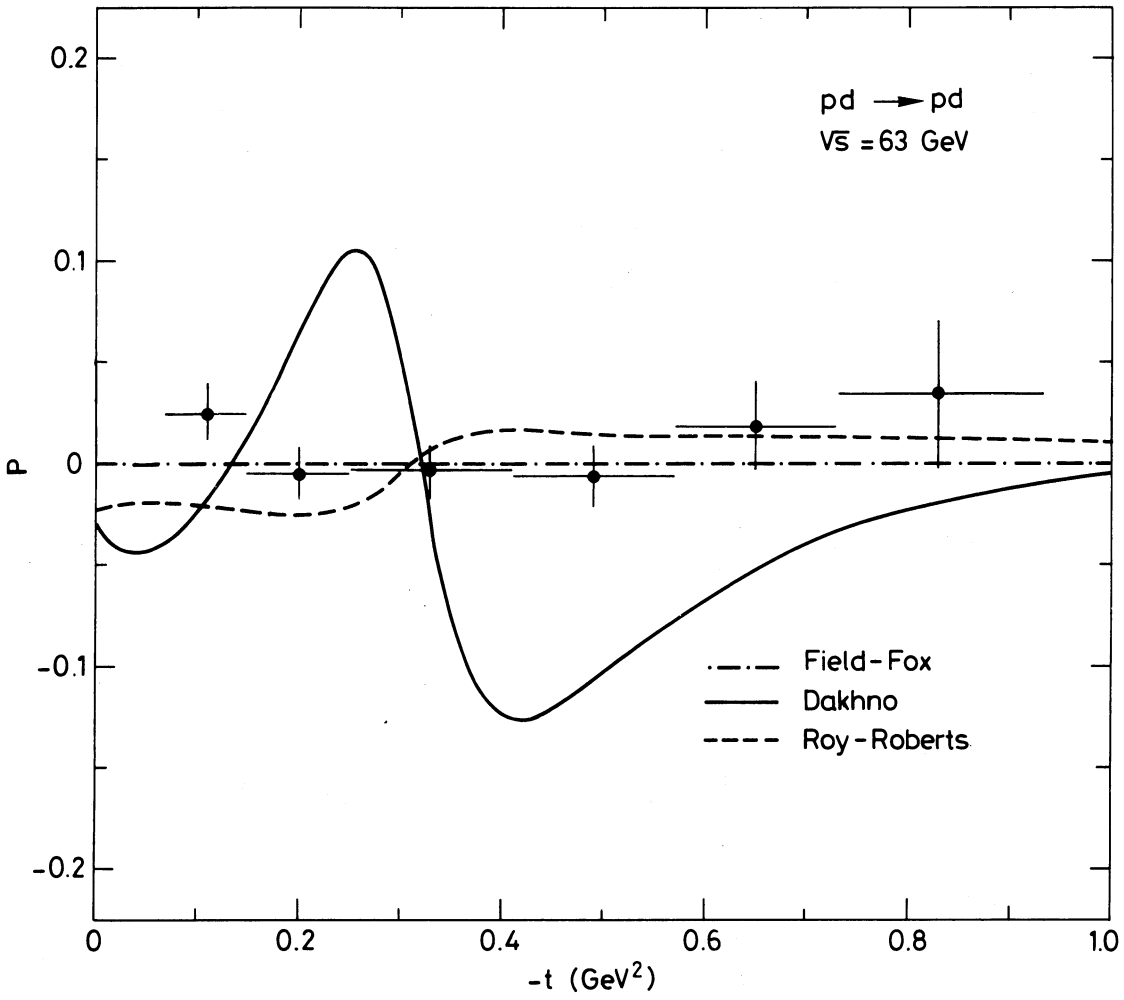
pd → pd
√s = 63 GeV
Field-Fox
Dakhno
Roy-Roberts
P
-t (GeV²)
0.2
0.1
0
-0.1
-0.2
0
0.2
0.4
0.6
0.8
1.0

Fig. 12

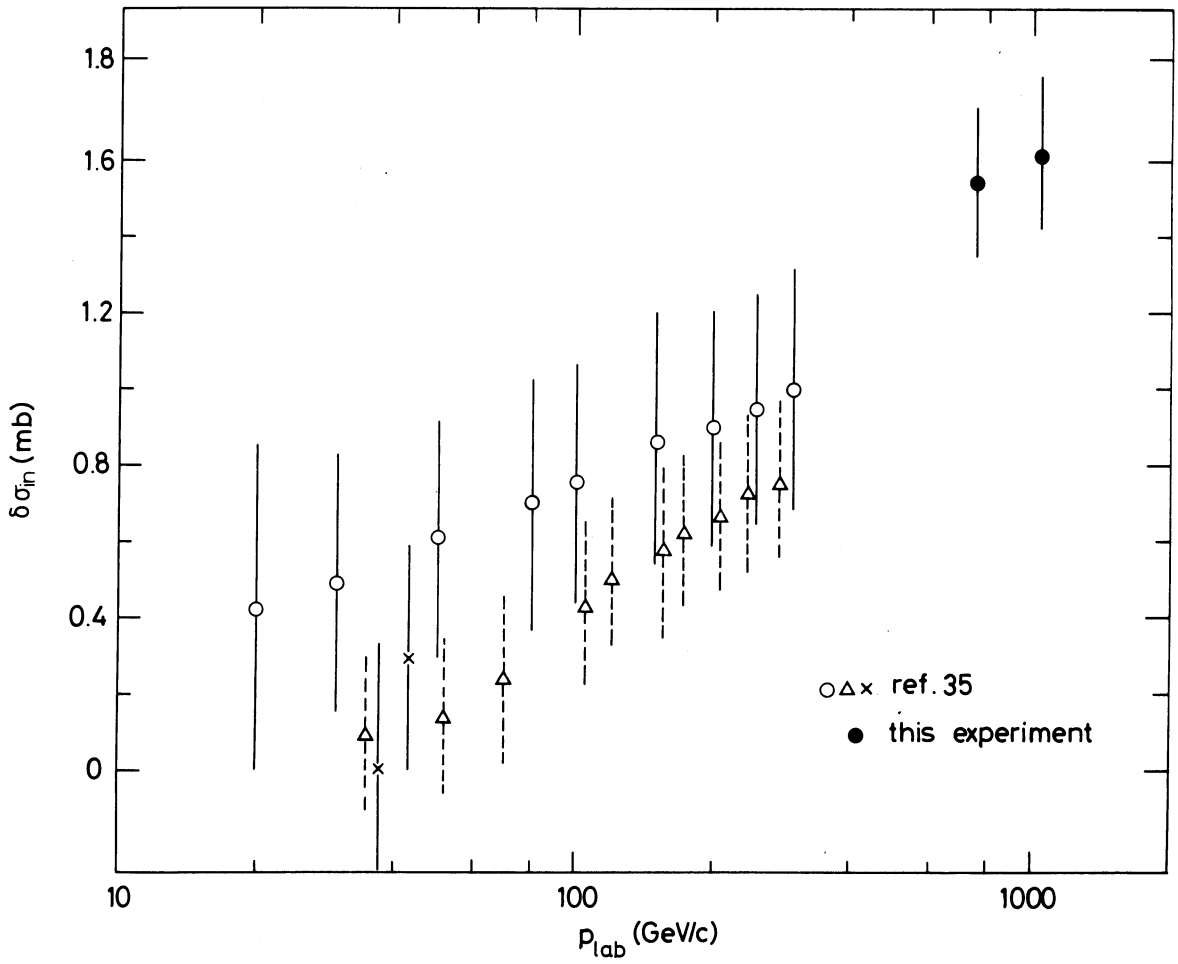
1.8
1.6
1.2
0.8
0.4
0
$\delta\sigma_{in}$ (mb)
10
100
1000
$p_{lab}$ (GeV/c)
○△× ref. 35
● this experiment

Fig. 13

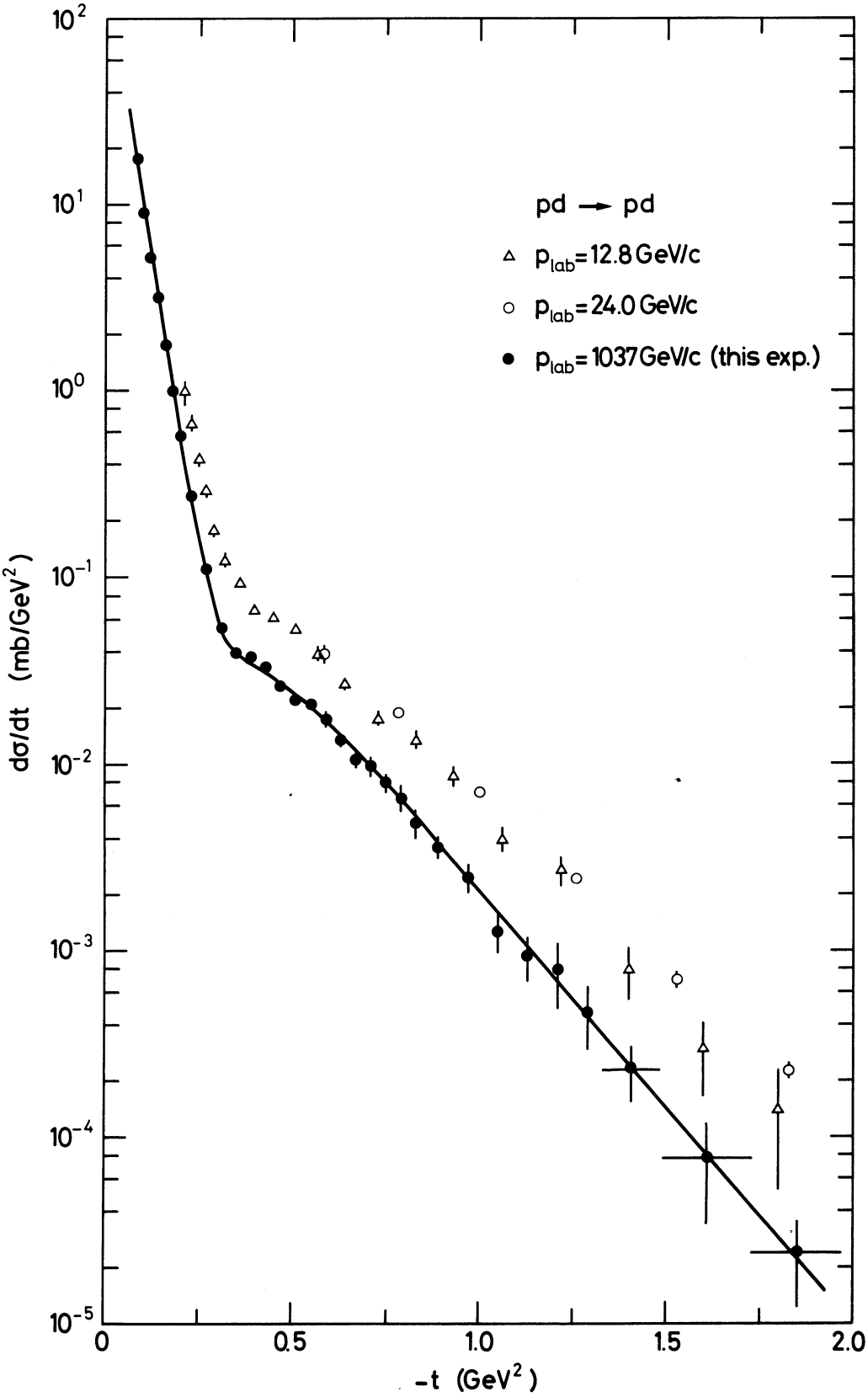
pd → pd
$p_{lab}$=12.8 GeV/c
$p_{lab}$=24.0 GeV/c
$p_{lab}$=1037 GeV/c (this exp.)
dσ/dt (mb/GeV$^2$)
-t (GeV$^2$)
$10^2$
$10^1$
$10^0$
$10^{-1}$
$10^{-2}$
$10^{-3}$
$10^{-4}$
$10^{-5}$
0
0.5
1.0
1.5
2.0

Fig. 14

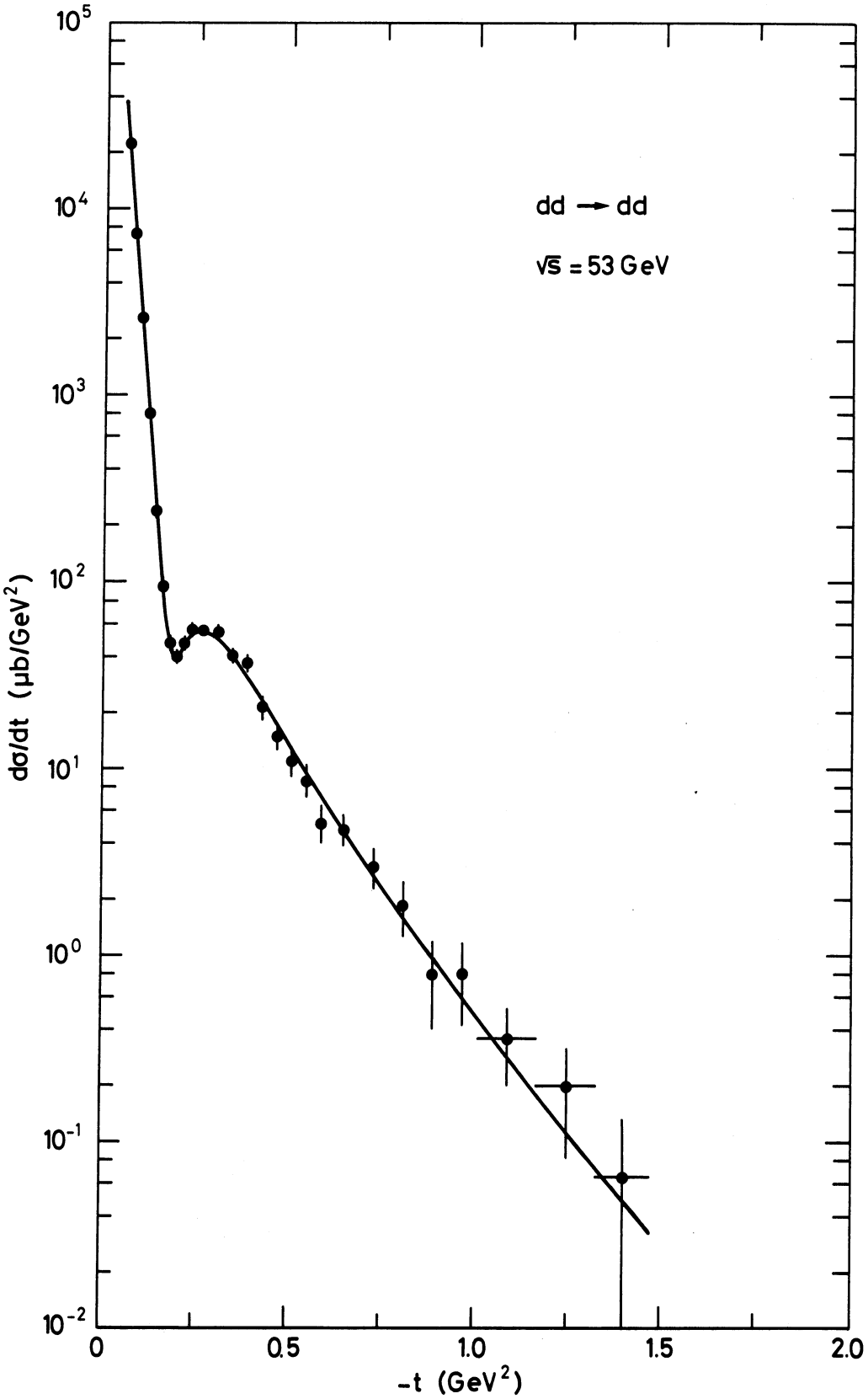
dd → dd
√s = 53 GeV
dσ/dt (μb/GeV²)
-t (GeV²)
10⁵
10⁴
10³
10²
10¹
10⁰
10⁻¹
10⁻²
0
0.5
1.0
1.5
2.0

Fig. 15

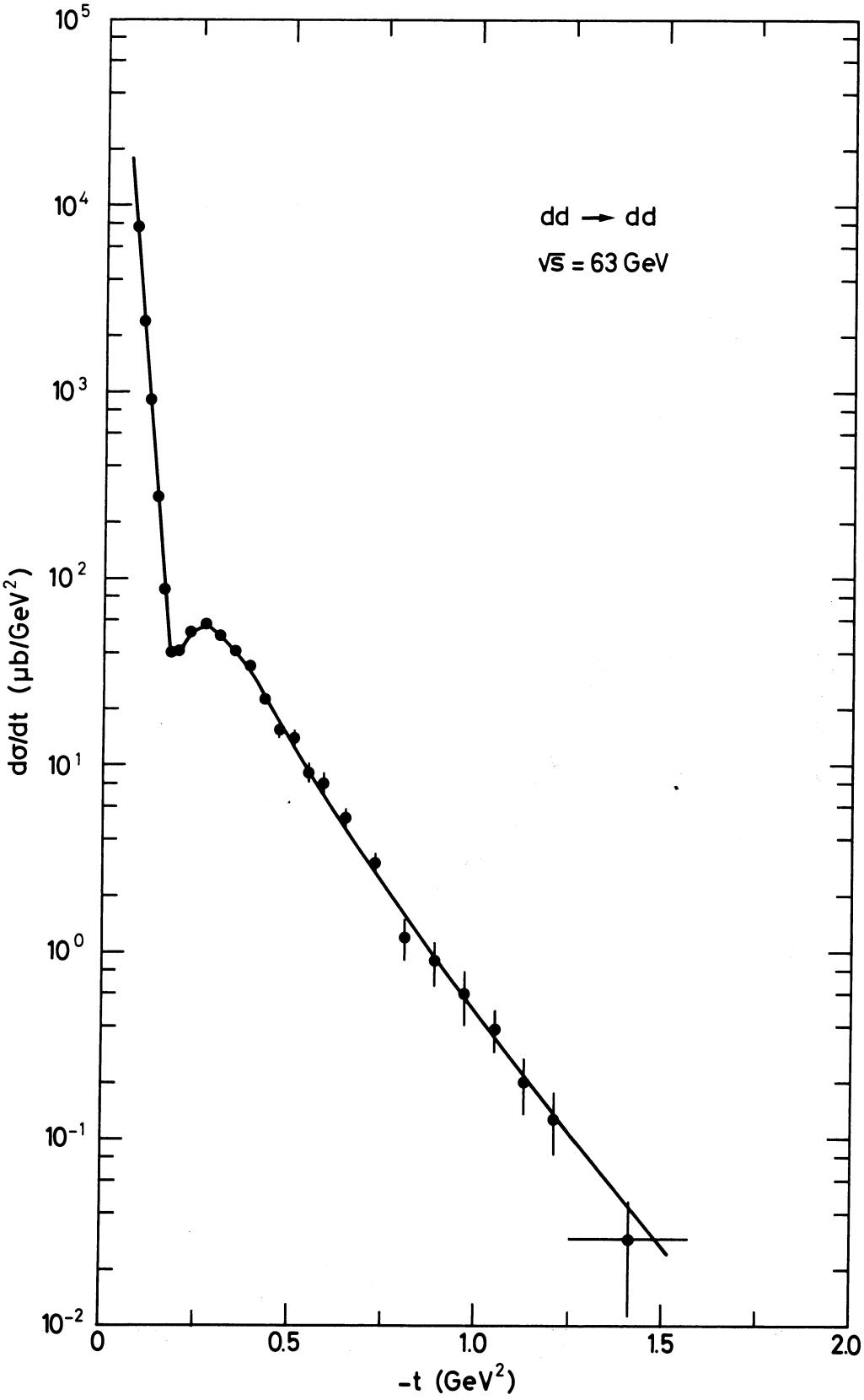
dd → dd
√s = 63 GeV
dσ/dt (μb/GeV²)
-t (GeV²)
10⁵
10⁴
10³
10²
10¹
10⁰
10⁻¹
10⁻²
0
0.5
1.0
1.5
2.0

Fig. 16

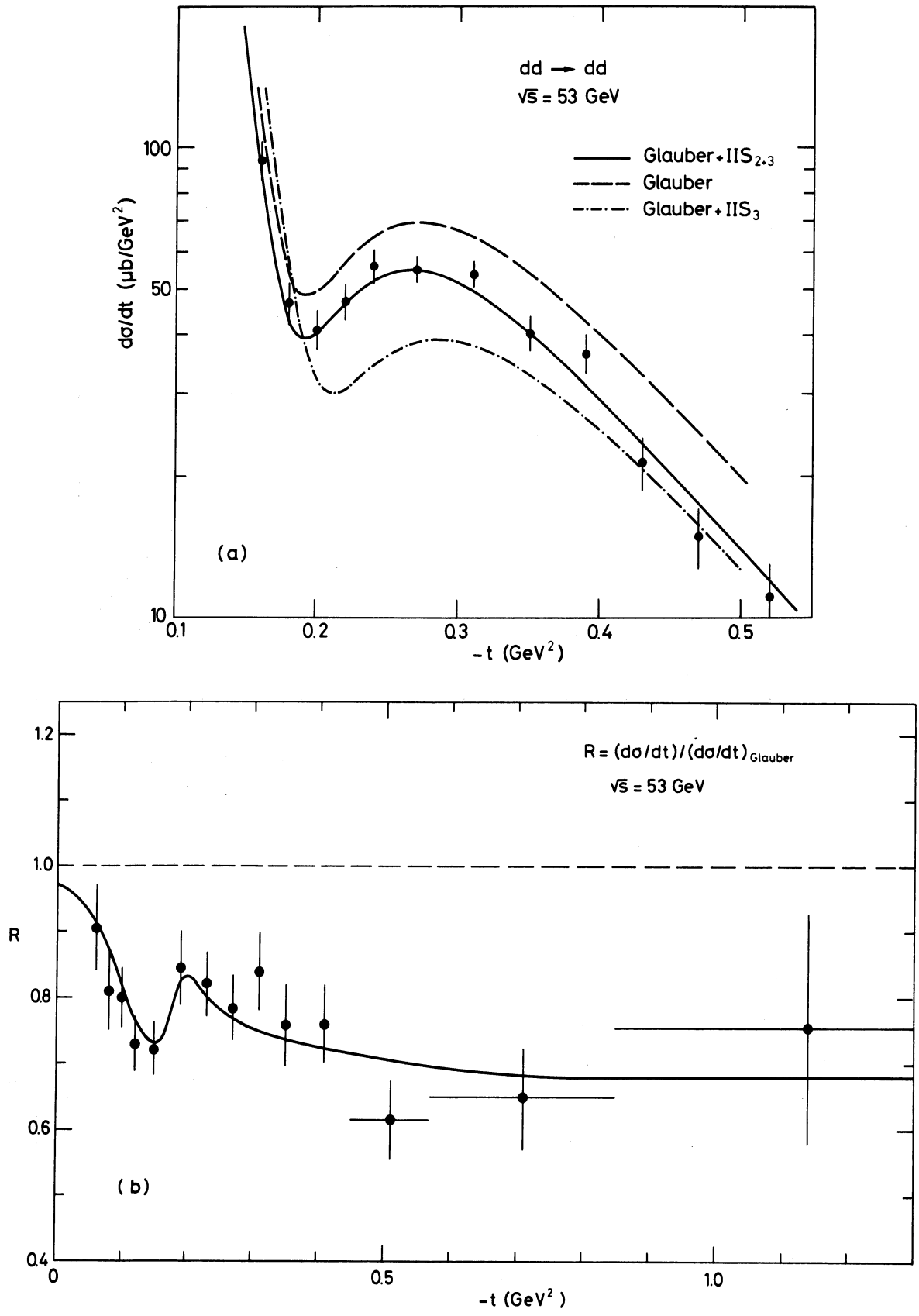
dd → dd
√s = 53 GeV
Glauber+IIS2+3
Glauber
Glauber+IIS3
(a)
dσ/dt (μb/GeV²)
100
50
10
0.1
0.2
0.3
0.4
0.5
-t (GeV²)
R = (dσ/dt)/(dσ/dt)Glauber
√s = 53 GeV
(b)
R
1.2
1.0
0.8
0.6
0.4
0
0.5
1.0
-t (GeV²)

Fig. 17

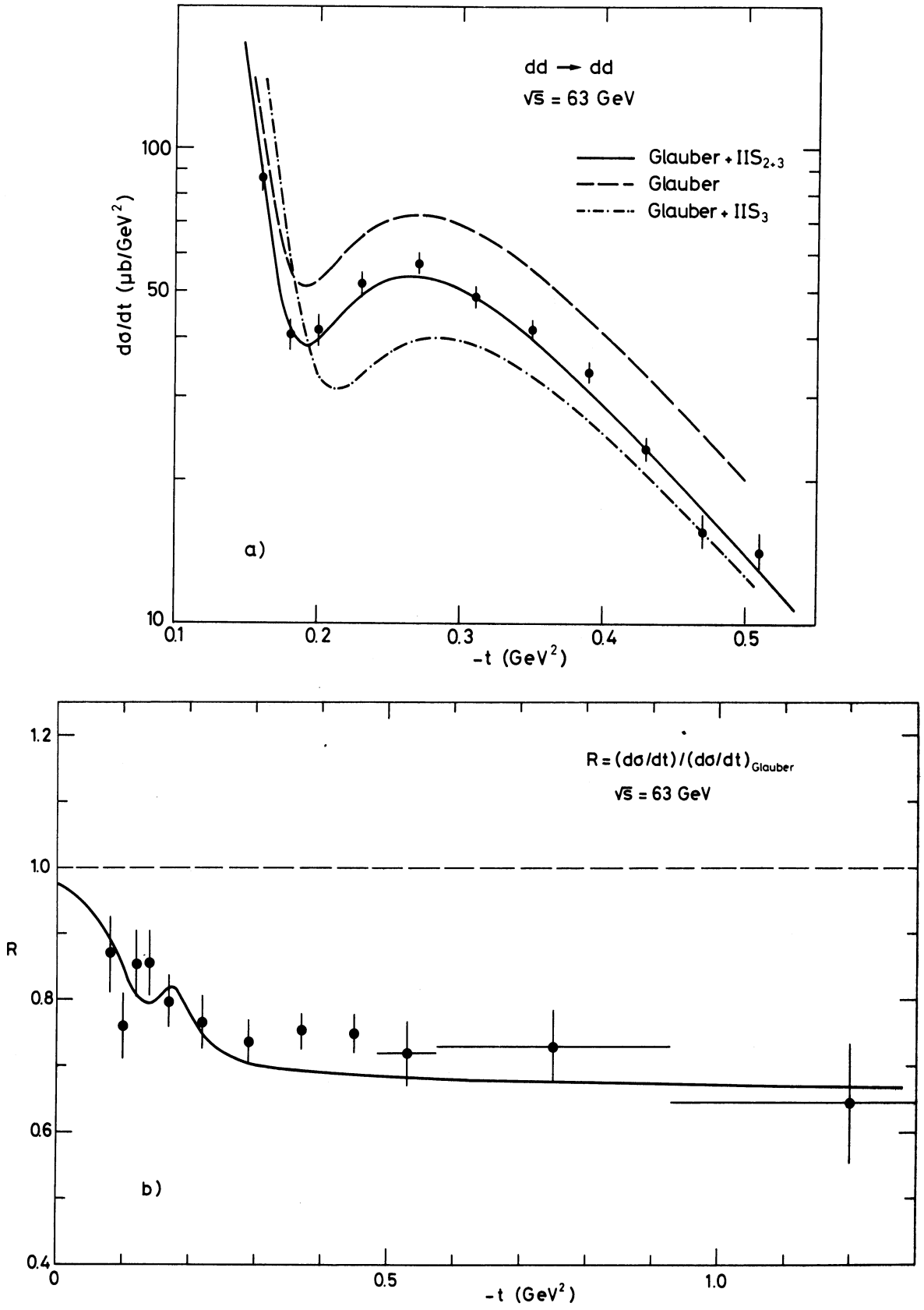
dd → dd
√s = 63 GeV
Glauber + IIS2+3
Glauber
Glauber + IIS3
a)
dσ/dt (μb/GeV²)
100
50
10
0.1
0.2
0.3
0.4
0.5
-t (GeV²)
R = (dσ/dt)/(dσ/dt)Glauber
√s = 63 GeV
b)
R
1.2
1.0
0.8
0.6
0.4
0
0.5
1.0
-t (GeV²)

Fig. 18

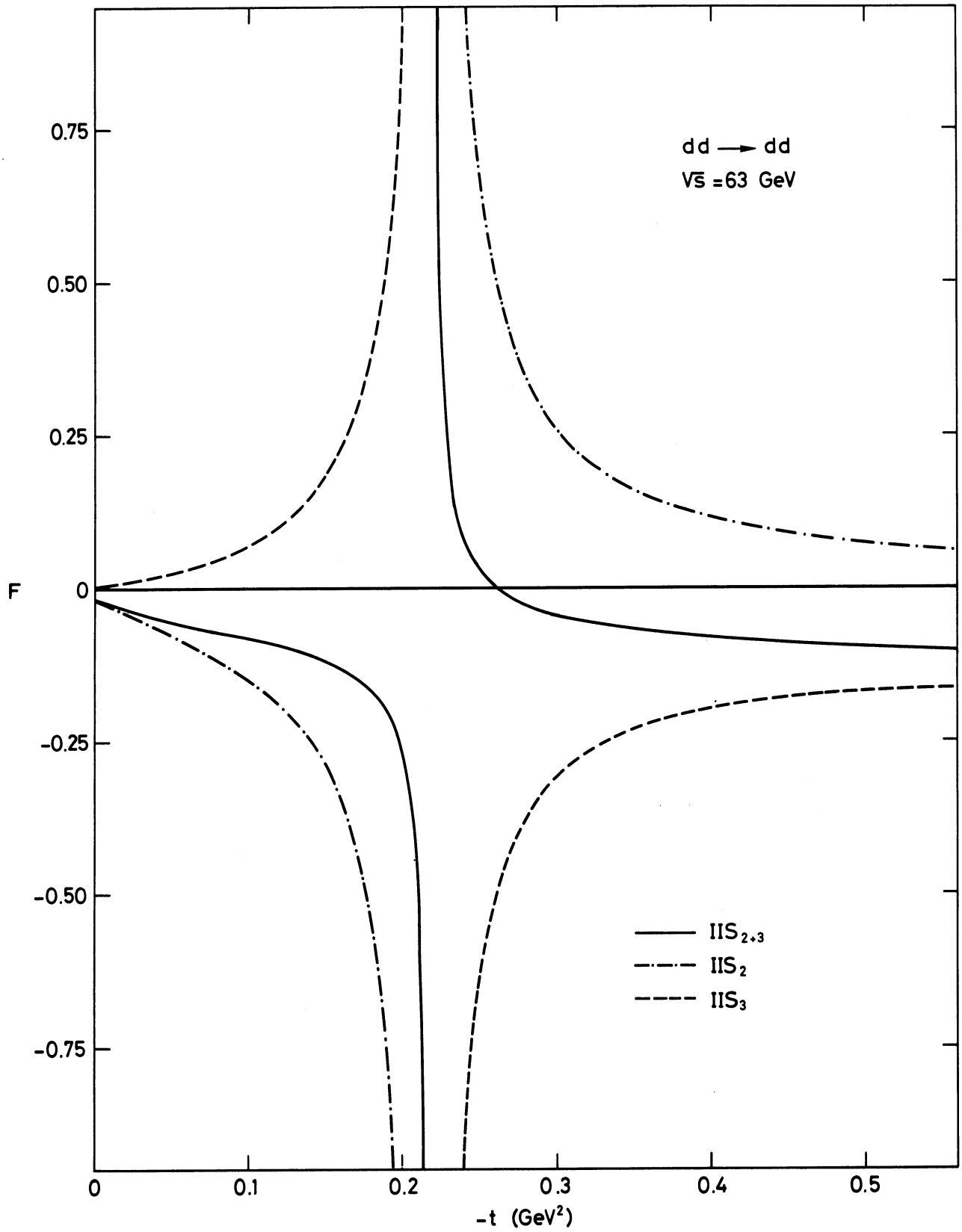
dd → dd
√s =63 GeV
0.75
0.50
0.25
F
0
-0.25
-0.50
-0.75
0
0.1
0.2
0.3
0.4
0.5
-t (GeV²)
IIS2+3
IIS2
IIS3

Fig. 19

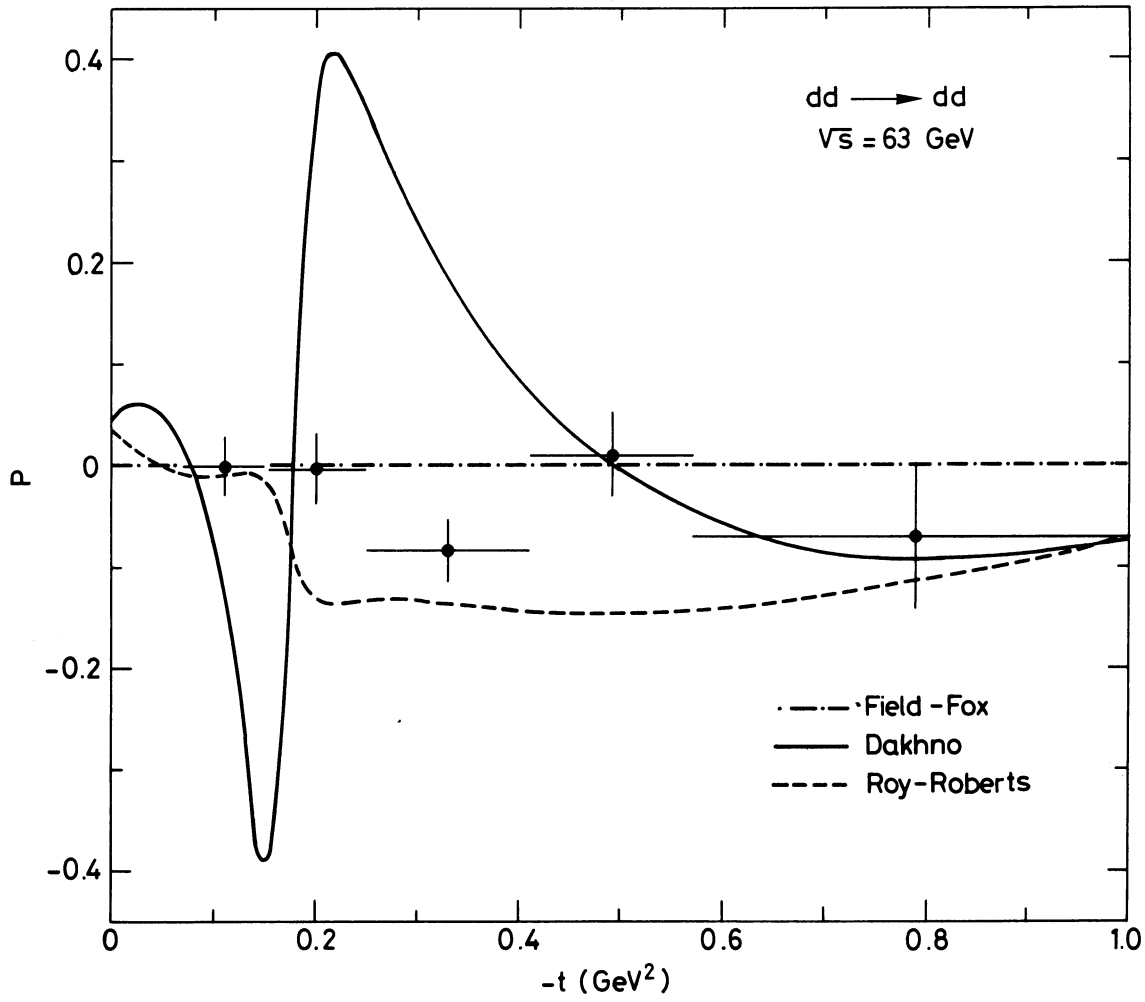
dd ⟶ dd
√s = 63 GeV
Field - Fox
Dakhno
Roy-Roberts
ρ
-t (GeV²)
0.4
0.2
0
-0.2
-0.4
0
0.2
0.4
0.6
0.8
1.0

Fig. 20

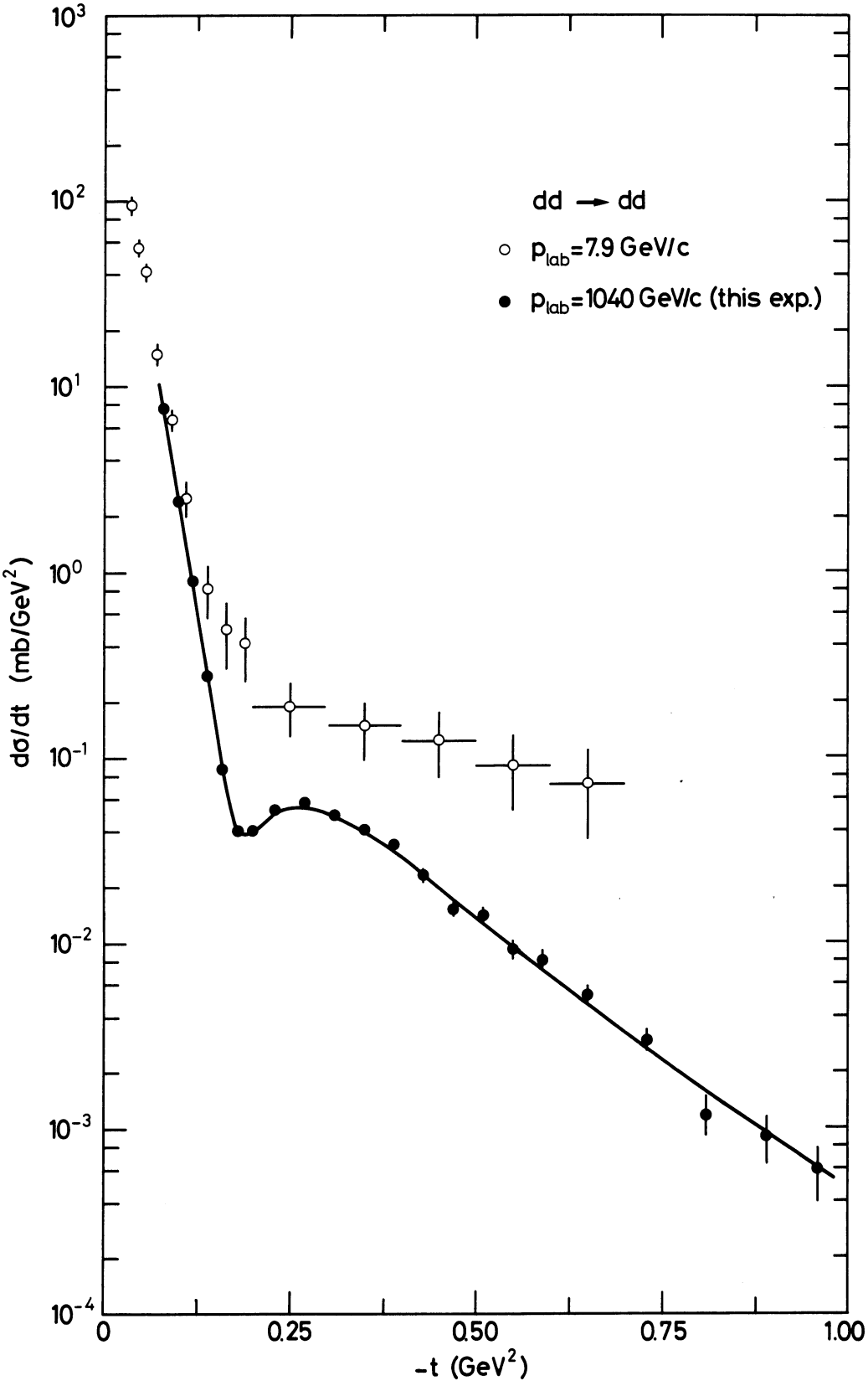
dd → dd
$p_{lab}$=7.9 GeV/c
$p_{lab}$=1040 GeV/c (this exp.)
dσ/dt (mb/GeV$^2$)
-t (GeV$^2$)
$10^3$
$10^2$
$10^1$
$10^0$
$10^{-1}$
$10^{-2}$
$10^{-3}$
$10^{-4}$
0
0.25
0.50
0.75
1.00

Fig. 21